

High-resolution large-eddy simulations of flow in a steep Alpine valley. Part I: Methodology, verification, and sensitivity experiments

Fotini Katopodes Chow¹, Andreas P. Weigel², Robert L. Street¹,
Mathias W. Rotach^{2,3}, and Ming Xue⁴

May 2, 2005

1: Environmental Fluid Mechanics Laboratory, Civil and Environmental Engineering,
Stanford University, Stanford, CA, USA

2: Institute for Atmospheric and Climate Science, Swiss Federal
Institute of Technology, Zurich, Switzerland

3: Swiss Federal Office for Meteorology and Climatology,
MeteoSwiss, Zurich, Switzerland

4: School of Meteorology and Center for Analysis and Prediction of Storms
University of Oklahoma, Norman, OK, USA

Corresponding author address:

Fotini Katopodes Chow
Department of Civil and Environmental Engineering
University of California, Berkeley
621 Davis Hall
Berkeley, CA 94720-1710
Phone: 1-510-643-4405, Fax: 1-510-642-7483
chow@ce.berkeley.edu

Abstract

This paper investigates the steps necessary to achieve accurate simulations of flow over steep, mountainous terrain. Large-eddy simulations of flow in the Riviera Valley in the southern Swiss Alps are performed at horizontal resolutions as fine as 150 m using the Advanced Regional Prediction System (ARPS). Comparisons are made to surface station and radiosonde measurements from the MAP-Riviera project field campaign of 1999. Excellent agreement between simulations and observations is obtained, but only when high-resolution surface datasets are used and the nested grid configurations are carefully chosen. Simply increasing spatial resolution without incorporating improved surface data gives unsatisfactory results. The sensitivity of the results to initial soil moisture, land use data, grid resolution, topographic shading, and turbulence models is explored. Even with strong thermal forcing, the onset and magnitude of the up-valley winds are highly sensitive to surface processes in areas which are well outside the high-resolution domain. In particular, the soil moisture initialization on the 1 km grid is found to be crucial to the success of the finer resolution predictions. High-resolution soil moisture and land use data on the 350 m resolution grid also improve results. The use of topographic shading improves radiation curves during sunrise and sunset, but the effects on the overall flow are limited because of the strong lateral boundary forcing from the 1 km grid where terrain slopes are not well resolved. The influence of the turbulence closure is also limited because of strong lateral forcing and hence limited residence time of air inside the valley, and because of the stable stratification which limits turbulent stress to the lowest few hundred meters near the surface.

1. Introduction

Increases in available computational power now allow high-resolution simulations of flow over complex terrain, but the appropriate numerical and physical parameters required by such simulations are not generally known. The influence of parameterizations such as those used for turbulence, soil moisture, solar radiation, surface roughness, the configuration of initial conditions, lateral boundary conditions, and the choice of numerical grids is highly situation dependent. Simulations are generally performed with “the best available” information and datasets. This paper investigates the steps necessary to achieve accurate large-eddy simulations of flow in highly complex terrain. Specifically, we examine the flow and temperature fields in the Riviera Valley, located in the Alps in southern Switzerland. The simulation results are verified through comparisons to surface and radiosonde observations in the Riviera Valley, obtained during the Mesoscale Alpine Programme (MAP) Riviera Project (Rotach et al. 2004). We also evaluate the model sensitivity to changes in parameterizations such as those listed above. The boundary layer processes in our simulated valley are described in Part II of this work (Weigel et al. 2005), which includes comparisons to aircraft flight data, descriptions of along-valley wind transitions and secondary cross-valley circulations, and a heat budget analysis.

Obtaining accurate simulations of flow in highly complex terrain has been the object of much research. At relatively coarse resolution, a large domain can be used, but steep mountains and valleys cannot be resolved. Benoit et al. (2002), for example, performed 14 km and 3 km resolution real-time simulations of the entire European Alps during the MAP special observing period. Lu and Turco (1995) and Jacobson (2001) simulated flow over complex terrain in California at approximately 5 km resolution. Many studies point to increased grid resolution as a means to achieve better agreement with observations (see e.g. Revell et al. (1996); Grønås and Sandvik (1999); Grell et al. (2000)). At finer resolution, the topography is better resolved but the slopes become steeper and the domain often has to be smaller, both of which create new computational problems. The simulations of Grønås and Sandvik (1999) of a narrow valley in Norway and of Revell et al. (1996)

of the New Zealand Alps region, for example, used resolutions down to about 250 m, but failed to reproduce the winds observed in the field, likely because they did not incorporate synoptic information or land surface data. More recently, Zhong and Fast (2003) compared simulations of the Salt Lake Valley region from three mesoscale models initialized with synoptic data. All three models (RAMS and MM5 at 0.56 km horizontal resolution, and Meso ETA at 0.85 km) were able to capture the general features of the valley flows as seen from observations. However, the details of the local circulations and vertical structure of the flow were not sufficiently well reproduced despite the relatively fine resolution used by these mesoscale models. The authors suggested that improvements in parameterizations of surface fluxes, vertical mixing, and radiation might further improve results.

Indeed, while the debate continues on whether increased resolution always increases the skill of weather forecasts (Hart et al. 2004; Cairns and Corey 2003), it must be recognized that merely increasing grid resolution does not necessarily address all deficiencies in numerical models or in model configuration. Chen et al. (2004) found that increasing the horizontal resolution (to 250 m) brought the most improvement to ARPS simulation results in the Salt Lake Valley region when the domain size was enlarged at the same time. Hanna and Yang (2001) suggested that errors in wind speed and direction in their simulations with four different mesoscale models were due to errors in the representation of turbulent motions, as well as to subgrid features in the topography and land use. Further examples are found in Zängl et al. (2004) and Gohm et al. (2004), who simulated Foehn winds in the Wipp and Rhine Valleys, respectively, with MM5. Despite using resolutions as fine as 267 m in the horizontal and two-way grid nesting to incorporate synoptic data, Gohm et al. (2004) found discrepancies between the simulations and observations; e.g., the model predicted a shallow Foehn wind occurrence that was not observed. The authors pointed to the need for higher-resolution representation of the topography outside of the fine resolution domain, because the coarse grids were unable to provide accurate lateral boundary condition forcing for the fine grids. Zängl et al. (2004) found that the effect of the horizontal computational mixing was larger than

the effect of increased resolution. Their model performed better with an improved computational mixing scheme at coarse resolution (3 km) than at fine resolution (1 km) with the traditional mixing scheme.

Previous simulations in the Riviera Valley region have been few. Grell et al. (2000) simulated a southern part of the Swiss Alps which included the Riviera Valley, using MM5 and RADM2 (for chemistry) with a horizontal resolution of 1 km to examine the advection of pollutants into Alpine valleys. Their focus was not on the Riviera, but on the neighboring Mesolcina Valley. Detailed comparison to observation data was not presented, and the authors stated that higher spatial and temporal resolution is needed to represent the atmospheric chemistry processes accurately. Simulations of the Riviera Valley, for the same time period as studied here, were performed by De Wekker et al. (2005) with the RAMS model (in Reynolds-Averaged Navier-Stokes, RANS, mode). Two-way grid nesting with grid spacings down to 333 m gave relatively good agreement with the observed potential temperature fields, but the numerical model did not capture the wind structure of the valley very well. Consistent up-slope and up-valley winds were not apparent. Our simulation setup has many similarities to that of De Wekker et al. (2005), as discussed below.

In this paper, we use large-eddy simulation (LES) to describe the flow structure over the highly complex terrain in the Riviera Valley with very fine resolution (as fine as 150 m horizontal spacing). Our simulation tool is the Advanced Regional Prediction System (ARPS), a non-hydrostatic, compressible large-eddy simulation code written for mesoscale and small-scale atmospheric flows (Xue et al. 2000, 2001, 2003). All the studies mentioned above used RANS formulations, not LES closures for their simulations. LES separates resolved and turbulent motions using a physical length scale, the width of the explicit spatial filter (Chow et al. 2005). RANS, on the other hand, applies a time average, usually with a very broad averaging period so that only very large scales are resolved. The traditional concept of LES is often associated with high-resolution simulations where most of the wavenumber range is resolved. The methodology of LES, however, does not prohibit its application to less well-resolved flows (Wyngaard 2004). The coarser grids in our nested

domain setup are more typical of mesoscale simulations, but can use the same LES equations. The differences between LES and RANS become small when similar space and time resolutions are used; often the only difference in implementation is the formulation of the turbulence model. The LES formulation is preferred for studies of turbulent flows because it is clear which physical features (length scales) are resolvable and which must be modeled. Wyngaard (2004) suggests the use of a more general tensor eddy-diffusivity model for coarser LES experiments; we have included a much more general dynamic reconstruction model (DRM) in our sensitivity experiments.

Simulations of the Riviera Valley are complicated by the complex terrain, the need for high-resolution surface datasets, and the presence of numerical discretization and lateral boundary condition errors, among other issues. The next section describes the flow conditions in the Riviera Valley on the days of interest, followed by a detailed description of our numerical setup (Section 3), and comparison of results to observation data (Section 4). We then perform sensitivity experiments to evaluate the relative impact of various configurations for soil moisture and temperature, land use data, grid resolution, topographic shading, and turbulence closure models (Section 5). We seek to answer several questions in the course of our study. Does increased grid resolution provide improved simulations? What are the effects of using high-resolution data for land use and soil properties? How are the results changed when topographic shading is included, or when different turbulence models are used? And finally, how do the nested grid parameters, such as size and resolution, affect the simulation results and/or the choice of physical parameterization schemes?

2. Flow conditions during the MAP-Riviera project

The Riviera Valley is a medium-sized valley located between the towns of Biasca and Bellinzona in the province of Ticino in southern Switzerland (see Figs. 1 and 2). The valley is about 15 km long and about 1.5 km wide at the valley floor, which is approximately 250 m asl at the southern entrance. Valley side walls have slopes of 30-35° and the surrounding peaks reach altitudes of up to 2700 m asl. The valley was the focus of an extensive field campaign, the MAP-Riviera Project

(Rotach et al. 2004), which was part of the larger Mesoscale Alpine Programme (MAP) conducted in the fall of 1999 (Bougeault et al. 2001). The field data include measurements from surface stations, radiosondes, and aircraft flights, among others.

The focus of the simulations in this work is on fair-weather days that are dominated by thermal forcing. On such “convective” days, a slope- and valley-wind system will develop within the valley and will be sensitive to the local surface conditions that determine heating and cooling. Inclusion of synoptic forcing is also necessary, however, especially because in the Alps, the flow is channeled along valleys that connect over a large domain. We have simulated the convective days of August 21, 22 and 25, 1999. We focus on August 25, 1999 in this paper because it was the most cloud-free day of the measurement campaign, and because wind data were missing from radio soundings on August 21 and 22. After determining the best simulation setup for August 25, where quantitative comparisons could be made for both wind and temperature fields, simulations of August 21 and 22 were performed. The results from August 21 and 22 and further analysis of the flow structure and the heat budget of the valley wind system for all three cases are given in Part II of this work (Weigel et al. 2005).

3. Numerical simulation setup

This section describes the procedures used to achieve accurate simulations of atmospheric flow in the Riviera Valley. The steps taken include the use of high-order numerical methods, carefully selected nested grids, high-resolution land surface data, modifications to the radiation model, and improved turbulence closure models. A standard procedure, with grid nesting, but without refined surface characteristics or soil moisture initialization, provides a reference against which enhanced simulations and sensitivity experiments are compared. Table 1 lists the configuration for various simulations.

a. *Large-eddy simulation code*

ARPS was developed at the Center for Analysis and Prediction of Storms at the University of Oklahoma, and is formulated as an LES code that solves the three-dimensional, compressible, non-hydrostatic, filtered Navier-Stokes equations. ARPS is described in detail by Xue et al. (1995, 2000, 2001, 2003), so we only mention the relevant settings for this application.

Fourth-order spatial differencing is used for the advection terms. Temporal discretization is performed using a mode-splitting technique to accommodate high-frequency acoustic waves. The large time steps (Δt) use the leapfrog method. First-order forward-backward explicit time stepping is used for the small time steps ($\Delta \tau$), except for terms responsible for vertical acoustic propagation, which are treated semi-implicitly. Simulations were performed in parallel (with message passing) on IBM SP Power4 processors.

b. *Grid nesting and topography*

Five one-way nested grids were used to simulate flow in the Riviera Valley at horizontal resolutions of 9 km, 3 km, 1 km, 350 m, and 150 m. The one-way nesting procedure used by ARPS allows adjustments in vertical resolution between grids, which we found to be necessary to accommodate the steep Riviera terrain; currently available two-way nesting schemes (in other codes) do not allow for vertical resolution changes, but the effect of two-way nesting should be explored in the future work. The valley first becomes reasonably well resolved at 350 m resolution (see the wavelet analysis of De Wekker 2002). Details of the simulation domains are listed in Table 2. Figure 2 shows the topography for the 1 km, 350 m, and 150 m subdomains. All grids are centered on the Riviera Valley at 46.2881 N, 9.002 E, except for the 150 m resolution grid which is centered at 46.275 N, 9.005 E. Thus the boundaries are placed as far as possible from our region of interest, minimizing contamination by errors at the lateral boundaries that are magnified when the boundaries cross through complex terrain (Warner et al. 1997). A Lambert conformal map projection is used with

the “true” latitude and longitude chosen very close to the center of the domain to minimize grid distortion, particularly for the smaller domains.

Topography for the 9 km through 1 km grids was obtained using USGS 30 arc second topography datasets. The 350 m and 150 m resolution terrain data were extracted from a 100 m dataset available for all of Switzerland (Volkert 1990). The terrain is smoothed near the boundaries of each nested subdomain to match the elevations from the surrounding coarser grid.

c. Vertical resolution and grid aspect ratio

ARPS uses a generalized terrain-following coordinate system. The grid is stretched using a hyperbolic tangent function from a vertical grid spacing of Δz_{min} at the surface to yield an average spacing of Δz_{avg} and a domain height of $\Delta z_{avg}(nz - 3)$ (see Table 2). The grid configurations are determined based on numerical considerations. High vertical resolution is needed to resolve the vertical structure of the atmosphere, especially near the earth’s surface, but if the grid aspect ratio ($\Delta x/\Delta z$) becomes too large, numerical errors become large, particularly in the horizontal gradient terms (Mahrer 1984). Poulos (1999) and De Wekker (2002) also found that the grid aspect ratio had to be small, especially for steep terrain. Increasing the vertical resolution too much, for example, leads to instabilities. Finally, LES also requires a small aspect ratio so as to avoid distortion of resolved eddies (Kravchenko et al. 1996).

Unfortunately, one or more of the above guidelines must be compromised because of the large domain sizes used here. At 9 km horizontal resolution, a good aspect ratio would require vertical resolution on the order of 1 km, but this would severely degrade the representation of the vertical structure of the atmosphere. Our chosen aspect ratio for the 9 km grid is 180 at the surface; with $\Delta z_{min} = 50$ m the vertical structure is reasonably well captured. For the fine grids, we have more flexibility because the horizontal resolution approaches the vertical resolution and we can construct a grid much more favorable for LES; therefore, our 350 m resolution grid has a much reduced aspect ratio of about 10.

d. Initialization and lateral boundary conditions

To obtain realistic initial and boundary conditions, data from the European Centre for Medium-Range Weather Forecasts (ECMWF) were used to force ARPS simulations at the lateral boundaries of the coarsest resolution (9 km) grid. ECMWF analyses are given at six-hour intervals with 0.5 degree (approximately 60 km) horizontal resolution and 50 vertical levels. The ECMWF initialization data compare fairly well with nearby soundings, e.g. in Milan, Italy and Payerne, Switzerland, located outside the Alps (see Fig. 1, soundings not shown), but because of poor vertical resolution cannot capture the pronounced inversion observed in the radio soundings on August 25 (see Fig. 8 later). The ECMWF data are applied at six-hour intervals and are linearly interpolated in between. Relaxation towards the boundary condition values is applied to a 5-10 grid-cell zone around the edge of the domain, depending on the grid. Simulations continued for 30 hours beginning at 1800 UTC August 24. Output at hourly intervals was used to provide initial and boundary condition files for subsequent nested grid simulations.

e. Surface characteristics

The characteristics of the land surface strongly influence sensible and latent heat flux exchanges with the atmosphere. Surface fluxes are particularly important for predicting thermally-forced flows such as slope winds and along-valley winds. The ARPS land-surface soil-vegetation model solves soil temperature and soil moisture equations, as described in detail in Xue et al. (1995, 2001). ARPS normally uses 13 soil types (including water and ice), and 14 vegetation classes (following the United States Department of Agriculture classifications). Land use, vegetation, and soil type data for the 1 km and coarser grids are obtained from USGS 30 second global data. The soil data pre-processing program of ARPS was modified to handle this finer resolution data.

For the 350 m and 150 m resolution grids, we enhanced the ARPS surface data classes to incorporate land use and soil type at 100 m resolution, available for all of Switzerland from the land use

and digital surface type data from the Swiss Federal Office of Statistics (GEOSTAT service). The dataset includes 69 land use categories; these have been mapped to a new set of 30 vegetation and 14 soil types (see Tables 8.3 and 8.4 and Fig. 8.4 in Chow 2004), as was done by De Wekker (2002) for RAMS. Different values, however, have been assigned in ARPS for the roughness length, leaf area index and vegetation fraction. A new soil type was added to represent bare rock, which makes up a significant portion of the mountain tops.

The soil-vegetation model must also be initialized with soil moisture and temperature data. Two soil layers of depths 0.01 m and 1.0 m for the surface and deep soil are used by the soil model. Soil temperature on the 9 km grid was initialized from ECMWF data. The soil temperature values at 9 km resolution are then interpolated to the 3 km and 1 km resolution grids. For the REF simulations (see Table 1), these ECMWF data are further interpolated to the 350 m grid. All other 350 m grids were initialized with a constant offset from the near-surface air temperature: 0.6 K for the top layer and -2.1 K for the deep soil. These offsets are based on field observations in the Riviera Valley.

The soil moisture initialization can be particularly important for thermally forced flows (Eastman et al. 1998). Soil moisture on the 9 km resolution grid was initialized from ECMWF data, which in the Alps range from 0 (rocky and glacial areas) to $0.37 \text{ m}^3 \text{ m}^{-3}$, with the deep soil slightly wetter than the top layer for this time period. The area near the Riviera Valley has values of about $0.35 \text{ m}^3 \text{ m}^{-3}$ (surface) and $0.366 \text{ m}^3 \text{ m}^{-3}$ (deep), except for the rocky outcroppings which are close to zero. As for the soil temperature, the ECMWF soil moisture values are interpolated to the 3 km grid. These ECMWF data are further interpolated to the 1 km and 350 m resolution grids for REF and REF-ST (see Table 1).

For LU-SM and other simulations (see Table 1), high-resolution soil moisture initialization data were obtained to represent the spatial variability in the Riviera Valley better. We followed De Wekker et al. (2005) and used the Water Flow and Balance Simulation Model (WaSiM-ETH) (Jasper 2001) to obtain soil moisture information. This hydrologic model is driven by meteorolog-

ical data such as air temperature and precipitation and provides 100 m resolution for the catchment region of the Riviera. Figure 3 shows the distribution of soil moisture for the two layers used at the 350 m grid level on August 24 at 1800 UTC. The soil moisture is highest on the valley floor, significantly lower on the steep surrounding slopes, and zero on the rocky peaks of the mountains and in urban areas (e.g. in Bellinzona and Biasca). In the upper soil level, the WaSiM moisture values are comparable to the ECMWF data ($\sim 0.32 \text{ m}^3\text{m}^{-3}$). At the deep soil level, where there are no plant roots to hold water, the WaSiM moisture on the steep slopes is very low ($0.08\text{-}0.12 \text{ m}^3\text{m}^{-3}$), but on the valley floor it is still relatively high ($\sim 0.25 \text{ m}^3\text{m}^{-3}$).

The soil moisture measurements taken at a few sites in the Riviera Valley during the field campaign (Zappa and Gurtz 2003) compare quite well with the WaSiM values. For example, at 1200 UTC, measurements at site A1 (see Fig. 2b) showed the soil moisture to be $0.318 \text{ m}^3\text{m}^{-3}$ at the surface and $0.293 \text{ m}^3\text{m}^{-3}$ at 25 cm depth. In contrast, site B showed $0.306 \text{ m}^3\text{m}^{-3}$ at the surface, and $0.212 \text{ m}^3\text{m}^{-3}$ at 25 cm depth. This near-constant moisture with depth on the valley floor and the significant decrease with depth on the slope also appear in the WaSiM data.

Given ECMWF data for the 9 km resolution grid and WaSiM data for the 350 m and 150 m grids, the question remains as to what the best values are at the intermediate resolutions of 3 km and 1 km. De Wekker et al. (2005) set the soil moisture to be constant on their coarser grids and found that the specific value did not significantly affect the results on the finest grid level. In contrast, our sensitivity studies in Section 5 show that soil moisture is a parameter to which the results are very sensitive, particularly at the 1 km grid level. We therefore incorporated a semi-empirical three-level soil moisture initialization, which is used for LU-SM on the 1 km grid. The soil moisture was set to 0 at altitudes above 2200 m where the soil type rock dominates. Between 2200 m and 500 m, moisture was initialized at $0.18 \text{ m}^3\text{m}^{-3}$, and below 500 m at $0.28 \text{ m}^3\text{m}^{-3}$. The same values were used at the surface and deep soil levels. These soil moisture values are intermediate values between the WaSiM deep and surface layer values, and can be seen as a compromise between the WaSiM and ECMWF data. The specific values were selected on a trial and error basis to obtain the

best results. In addition to using interpolated ECMWF and three-level soil moisture initializations, we investigated the use of WaSiM data outside the Riviera catchment area in the LU-SM2 setup. The three choices for soil moisture initialization for the 1 km grid are summarized in Table 3 and are discussed further in Section 5a.

f. *Radiation model*

In steep valleys, “topographic shading” from shadows cast by neighboring topography can be important. ARPS normally only includes the effect of surface inclination when calculating incoming solar radiation. This “self-shading” accounts for much of the required modification to the incoming radiation in complex terrain, but topographic shading must be included to properly represent surface heating during sunrise and sunset. We use the topographic shading method of Colette et al. (2003), which is included in the latest version of ARPS. Colette et al. (2003) found that the inclusion of topographic shading could delay the morning inversion layer breakup in idealized simulations with steep valleys by approximately half an hour. The field study of Matzinger et al. (2003) emphasized the importance of the topographic shading in the Riviera Valley, where the delay in local sunrise significantly alters the net radiation balance. We evaluate the effect of topographic shading in Section 4d. The complete treatment of short- and long-wave radiation in ARPS is described in Xue et al. (2001).

g. *Turbulence and computational mixing*

The standard closure models in ARPS include 1.5-order TKE (Deardorff 1980; Moeng 1984) and static Smagorinsky-Lilly models (Smagorinsky 1963; Lilly 1962). The TKE-1.5 model solves an equation for the turbulent kinetic energy to determine the velocity scale for use in an LES-type eddy-viscosity formulation. The model can be used for LES as long as the chosen length scale is proportional to the filter width, as is done in ARPS (Deardorff 1980; Moeng 1984). The TKE

approach is especially useful when a large fraction of the velocity scales is contained in the subfilter scales, as for coarse resolution grids (Pope 2000, Chapter 13).

The TKE-1.5 closure is used in most of our simulations, but the dynamic reconstruction model (DRM) of Chow et al. (2005) has also been applied at the 350 m grid. The DRM is a mixed model, combining a high-order scale-similarity term with a dynamic eddy-viscosity model. Here we use the Bardina scale-similarity term together with the dynamic model of Wong and Lilly (1994). Further details about the model and its implementation over complex terrain can be found in Chow (2004, Chapter 8). Simulations of neutral boundary layer flow using DRM over flat terrain were able to accurately represent the expected logarithmic layer near the bottom boundary, unlike standard eddy-viscosity models (Chow et al. 2005). Applications to flow over an isolated hill (Askervein Hill, Scotland) were also successful (Chow and Street 2004). Here, the DRM is also applied to the transport equation for potential temperature.

In addition to the turbulence model, fourth-order computational mixing (applied in computational space) is used to damp high-frequency motions that can build up due to nonlinear interactions; this can be considered a type of hyper-viscosity. ARPS also includes a divergence damping term to control acoustic noise. The impact of both of these damping terms has been investigated and the coefficients have been set to give the minimum amount of mixing required for stability.

4. Verification and comparison with observation data

Detailed results comparing the REF and LU-SM simulations with observation data for August 25, 1999 are given in this section. All results are from the 350 m resolution grid unless otherwise noted. The 150 m grid data are used in Part II to calculate profiles of the heat budget components over the valley base (Weigel et al. 2005).

a. Surface temperature and wind time series

Typical thermally-driven valley wind patterns include the onset of up-slope winds on the valley walls in the morning and the development of up-valley winds during the day. In the evening, the winds transition to down-slope and down-valley directions. The heating mechanisms which drive the Riviera Valley wind transitions are evaluated in detail in Part II (Weigel et al. 2005). A comprehensive discussion of slope and valley winds can be found in Whiteman (2000). The winds in the Riviera exhibit some aspects of typical valley flow patterns, as described further below.

Figure 4 shows the evolution of the surface potential temperature (θ) on August 25 at site A1 (Bosco di Sotto, see Table 4 and Fig. 2b) near the center of the simulation domains. Surface and radiosonde observations were collected at this location during the field campaign. The observations are compared to the REF, REF-ST, and LU-SM results. To further quantify the comparison, the first three rows of Table 5 show the root-mean-square errors (rmse) and mean errors (bias) between simulations and surface observations at site A1. They are defined:

$$\text{bias} = \frac{1}{M} \sum_{j=1}^M \frac{1}{N} \sum_{i=1}^N (A_{i,j} - B_{i,j}) \quad (1)$$

$$\text{rmse} = \sqrt{\frac{1}{M} \sum_{j=1}^M \frac{1}{N} \sum_{i=1}^N (A_{i,j} - B_{i,j})^2} \quad (2)$$

where M is the number of time steps, N is the number of grid points, and $A_{i,j}$ and $B_{i,j}$ are the values of the datasets being compared.

From Fig. 4, we see that REF strongly underpredicts surface temperatures by up to 6 K (with an rmse of 3.20 K) while LU-SM stays within less than about 1 K from the observations (rmse of 0.69 K). After further investigation at the suggestion of one of the reviewers, the difference between the surface temperature in REF and LU-SM was found to be mostly due to the soil temperature initialization. REF uses soil temperature fields interpolated from ECMWF data, which are almost uniform over the 350 m Riviera Valley domain. LU-SM, on the other hand, uses an offset from the air temperature to initialize the soil temperature on the 350 m grid, and thus has elevation-dependent values which are more realistic and provide improved agreement with the observations.

This hypothesis was verified by REF-ST, which uses the REF setup except that we initialized the soil temperature with an offset like in LU-SM, giving a reduction in rmse from 3.20 K (REF) to 1.60 K (REF-ST). The REF-ST setup required a simple code modification from the standard initialization options available in ARPS and showed the importance of spatial variability in soil temperature in complex terrain. All simulations except REF use the temperature offset to initialize the soil temperature (see Table 1). Because of the large temperature bias in REF, subsequent comparisons are made between REF-ST (rather than REF) and LU-SM, so as to isolate further differences in the model runs.

Figure 5 shows the evolution of surface wind speed (U) and direction (ϕ), also at site A1. During the first 6-7 hours on August 25, the dominant winds were down-valley (about 330°). Between 0600 and 0800 UTC (local time is CEST (Central European Summer Time) = UTC + 2 hours), winds shift to up-valley (about 150°). Local sunrise is at approximately 0700 UTC at the valley floor, but is earlier on the east-facing slopes and in the Magadino Valley (see Fig. 2). Sunset is at approximately 1600 UTC, and the winds shift to down-valley starting at about 1800 UTC. The surface winds are generally weak at night and become stronger with the onset of the up-valley flow during the day.

Comparisons with observations are now only shown for REF-ST and LU-SM for simplicity (the wind speed for REF-ST is similar to REF), but the rmse and bias values in Table 5 also include REF. The LU-SM predictions of the wind speed in Fig. 5 show the onset of up-valley winds about 1 to 2 hours later than observed at site A1, but this is significantly better than both REF-ST and REF. While the surface wind speed rmse values at site A1 are similar for all three simulations, the rmse does not reflect the fact that the wind transition delay in up-valley winds is 3-4 hours for REF-ST and 4-5 hours for REF. The ARPS data in the surface time series are from the lowest model level, which for the horizontal winds and temperature is at $\Delta z_{min}/2$ (15 m for the 350 m grid; see Table 2). Comparison is usually made to the closest observation level, but there can be surface layer effects due to the plant canopy, which is not represented in the model, so comparisons

to a higher measurement level are often better. At site A1 we take an average of the observations at 15.9 and 28 m agl. The wind direction is not representative of the diurnal valley flows when winds are weak, making comparisons with LES results difficult. Nevertheless, the surface wind direction and speed are reproduced quite well by LU-SM. The results of De Wekker et al. (2005) showed a 2-hour delay in the onset of the up-valley winds and did not capture the evening transition to down-valley winds.

Overall, the errors between the observations and the simulated fields at site A1 from LU-SM are quite small in the Riviera Valley (e.g. rmse of ~ 0.7 K for potential temperature and ~ 1.3 m/s for wind speed), especially when compared to the results of other typical simulations (Zängl et al. 2004; Zhong and Fast 2003). LU-SM significantly reduces all the errors except the wind direction bias, where REF-ST exhibited more fluctuations and hence a lower overall bias. Wind direction errors are large because of the fluctuations present at low wind speeds.

The most likely reason for the delayed along-valley wind transitions in the ARPS simulations is poor representation of surface soil conditions. Soil moisture controls the partitioning of surface heat fluxes into sensible and latent fluxes, thus determining the heating and cooling of the surface and ultimately the strength of along-valley and slope winds. Sensitivity tests in Section 5a confirm that changes in the soil moisture can significantly change the onset of valley wind transitions. Sensitivity to the soil temperature offset used for initialization in all runs except REF was small, and therefore was not investigated further.

The surface observations at the valley floor provide a simple reference for evaluating the simulation results, but we compare results at additional sites because the complex topography can lead to different wind transitions at different locations. Figures 6 and 7 show observed and simulated winds at surface stations at site C (Pian Perdascio, east-facing slope) and site E2 (Monte Nuovo, west-facing slope) (see Fig. 2b). Quantitative errors are given in Table 5 for these and two other sites on the eastern slope (B, E1). Note that the measured and simulated wind directions indicate the up-slope and down-slope transitions along the slopes and not the up-valley/down-valley direc-

tions as at site A1. Comparisons along the slopes are often difficult because of the effect of the plant canopy (Van Gorsel et al. 2003), and can be very sensitive to the exact location chosen on the grid; moving 100 m to the east or west can change the elevation by almost 100 m.

b. Vertical profiles

Figure 8 compares the potential temperature, wind speed, wind direction, and specific humidity (q) simulated by REF-ST and LU-SM with radiosonde data from site A1. The temperature structure of the atmosphere early in the morning (0739 UTC) is characterized by a stable layer below 1.5 km asl, a very stable layer between 1.5 and 2.2 km asl, and a mixed or slightly stable layer above that extends to about 4.5 km asl. The strong capping inversion at about 2 km asl is also present in the synoptic flow and is likely due to large-scale subsidence near a regional high pressure system; soundings well outside of the Alps in Milan, for example, also exhibit this inversion. Typical valley inversion layer breakup theory predicts that the mixed layer will continue to grow while there is surface heating, as on such a “convective” day, and will eventually extend over the entire valley depth (Whiteman 2000). The radiosonde observations, however, only show an 800 m mixed layer near the ground at 1208 UTC. The valley atmosphere above remains stable. The fact that the evolution of the vertical structure is atypical can be seen further from the sounding at 1508 UTC, when the surface temperature has increased by another degree but the mixed layer depth has decreased to about 500 m. This indicates the presence of other processes which act to inhibit mixed layer growth. The persistence of the stable layer throughout the day may be due to the presence of a strong secondary circulation and subsidence warming in the valley; these features are particularly evident on August 21 and 22, and have been discussed by Weigel and Rotach (2004) and are analyzed in more detail in Part II (Weigel et al. 2005).

The agreement between LU-SM and the observed profiles in Fig. 8 is much better than REF-ST which does poorly near the ground. In particular, the potential temperature from REF-ST exhibits a cold bias below 1 km asl. The REF-ST wind direction also fails to exhibit the observed up-valley

flow at 0915. Our simulated profiles are taken from one instant at the hour or half hour closest to the radiosonde ascent time, and are interpolated horizontally to the launch location. In the afternoon, the observed wind profiles corroborate the measurements at the surface stations which show increased wind speeds during the up-valley wind period. Both simulations, however, fail to match the observed surface warming during the afternoon, particularly at 1508 UTC. The wind speed profiles are especially difficult to compare because observed winds depend on fluctuations of the radiosonde's position as it rises. We cannot expect the LES results to provide exactly the same instantaneous profiles, but rather to represent the "mean" or resolved-scale structure (Germano 1996). Another significant discrepancy between the observations and the simulation results is found at 2118 UTC, when the inversion at 2 km asl sharpens; the simulations do not resolve this feature in the temperature or humidity profiles. Wind data at 2118 UTC are missing near the surface, but the simulations indicate that the winds have reversed to down-valley, in agreement with the surface station time series observations (Fig. 5).

Table 6 shows the rmse and bias errors for LU-SM for each profile, including data up to about 6 km asl; the errors are quite small (e.g. ~ 2 m/s for wind speed) and confirm the good agreement between simulations and observations seen visually. Table 6 also gives the rmse and bias over all sounding times for REF and REF-ST, showing the overall improvement for LU-SM (e.g. θ rmse decreases from 1.43 to 0.94 K, and U rmse decreases from 2.29 to 2.04 m/s, from REF to LU-SM). The results of De Wekker et al. (2005) showed good surface temperature agreement at 0915, 1208 and 1508 UTC, but further above the ground the modeled profiles were too smooth and did not compare as well with observations as our LU-SM results. Specific humidity is also better reproduced in our simulations. It is difficult to compare wind predictions directly as De Wekker et al. (2005) presented vector profiles instead.

c. *Surface heat and momentum fluxes*

Surface fluxes in ARPS are calculated from similarity theory, and they provide the necessary surface heating and cooling to drive valley winds. Figure 9 shows the modeled and observed time series of the sensible heat flux at surface stations A1 (valley floor) and B (eastern slope) for REF-ST and LU-SM; these stations are chosen to highlight differences between fluxes on the valley floor and slopes and because data were available and of good quality. The heat flux is the kinematic heat flux defined as $\overline{w\theta}$, where the overbar denotes spatial averaging. The heat fluxes from LU-SM compare quite well to the observations, especially considering the high spatial variability observed in the valley due to local slope variations (De Wekker 2002, Fig. 2.10). The REF-ST results predict less than half the peak magnitude of the observed heat fluxes, thus reflecting the influence of soil moisture on surface heating and the consequently delayed onset of the up-valley winds. Station B on the east slope exhibits stronger negative heat fluxes at night than station A1 (0000 to 0700 UTC). Significant positive heat fluxes are observed during the day at both sites, with the simulations giving higher values at the valley floor than observed during the latter half of the afternoon. The peak heat flux is delayed on the east slope relative to the valley floor because the slope does not receive direct sunlight until later in the morning, and is heated until later in the afternoon. The peak magnitude is also much larger at site B because of the surface inclination and exposure of the site in the afternoon.

d. *Radiation budget*

The simulated surface heating depends on accurate representations of the incoming and outgoing radiation. Figure 10 shows the surface radiation balance throughout the day from LU-SM as compared to measurements at surface station A1. (Differences for REF-ST are quite small and therefore not shown.) The model slightly overpredicts incoming shortwave radiation, probably due to aerosols present in the Riviera atmosphere that are not accounted for by the model. The dip

in the observations at 1300 UTC was due to a brief period of clouds which was not captured in the simulations. The net radiation is slightly underpredicted day and night, which implies that the longwave radiation balance is at fault. Zhong and Fast (2003) found that night-time net radiation was also too low in their simulations of Salt Lake Valley. The net longwave radiation is often thought to be underestimated in valleys because the radiation models are one-dimensional (in the vertical); the models do not account for the incoming longwave emissions from the valley walls at night and therefore allow too much cooling.

The bias in our model values may be due to a combination of effects. Surface radiation measurements in the Riviera Valley showed that incoming longwave radiation was about 20-50 W/m² larger on the valley floor as compared to on the ridge of the valley (Matzinger et al. 2003), indicating the effect of heating from the side walls. There were also particularly high daytime concentrations of aerosols on 25 August which could affect the downward longwave radiation. Finally, the choice of the constant surface emissivity in ARPS (0.995) may be too high (e.g. compared to the value used by Whiteman et al. 2004); we leave this to further investigations. Zhong and Fast (2003) also suggest that the absence of topographic shading in their simulations caused discrepancies; this effect is examined in Section 5d.

e. *Vertical turbulence structure*

Figure 11 shows vertical cross sections of the resolved and subfilter-scale (SFS) turbulent stress contributions from LU-SM for vw averaged from 1300 to 1500 UTC at 300 s intervals. The vertical slice is perpendicular to the valley axis at site A1 (see Fig. 2). The velocities have been rotated to be aligned with the valley axes so that u is cross-valley (to the north-east) and v is along-valley (to the north-west); the uw stresses (not shown) have a somewhat lower magnitude. The resolved stress is computed from $\langle vw \rangle_{res} \equiv \langle \bar{v} \bar{w} \rangle - \langle \bar{v} \rangle \langle \bar{w} \rangle$ where the brackets denote time averaging. The plotted SFS stress is $\langle \tau_{23} \rangle$, which contributes significantly only below about 500 m; here, the SFS stresses are several times larger than the resolved stresses, as also seen in the

vertical profiles at the valley floor in Fig. 12. Profiles from the REF-ST simulations (not shown) are considerably lower in magnitude because of the reduced surface fluxes (Fig. 9). The atmosphere in the Riviera is stably stratified throughout the day except very near the surface (see Fig. 8), and the TKE-1.5 closure will not produce SFS turbulence when the flow is stable (as measured by the Richardson number) or when the shear is too weak. That the SFS stress contributions are not large outside the near-surface layer perhaps explains why using different turbulence models does not have very large effects (see Section 5e).

5. Sensitivity tests

The comparisons in Section 4 contrasted the improved results from LU-SM with those from REF-ST which used a standard procedure with standard initial conditions and surface datasets. The LU-SM setup includes all the components found necessary to give the best agreement with observations. We now examine the effects of individual pieces used in LU-SM to determine the significance of each. We also attempt to provide some general recommendations for future simulations over complex terrain.

a. *Soil moisture*

Several studies have found sensitivity of simulation results to soil moisture (e.g. Eastman et al. 1998; Chen et al. 2001). The improved results from the use of high-resolution WaSiM soil moisture data have been shown in Figs. 5-8 which compare REF-ST and LU-SM. REF-ST used ECMWF soil moisture data; the result was that the up-valley wind transition occurred too late (by 3-4 hours) throughout the entire nested set of grids. Banta and Gannon (1995) found that increased soil moisture decreases the strength of katabatic winds; this is due to slower cooling caused by the increased thermal conductivity of moist soil and increased downward longwave radiation (because the air near the surface has higher humidity). Ookouchi et al. (1984) showed that increased soil

moisture decreases up-slope winds because the wetter soil does not heat as quickly and hence produces smaller horizontal pressure gradients. Accordingly, with wetter soil (REF-ST), the transition to up-valley winds begins later, while the slightly drier soil (LU-SM) better reproduces the transition. This simple explanation is complicated, however, by the complexity in the topography of the Riviera Valley and its tributaries (the Magadino, Mesolcina, Leventina and Blenio Valleys), because the effect of soil moisture will be different in each valley. Strong down-valley winds from the Mesolcina Valley, for example, could block the entrance of up-valley winds from the Magadino Valley into the Riviera Valley.

That the soil moisture effect is not straightforward is demonstrated by another experiment in which we use the WaSiM data at coarse resolutions as well. The WaSiM data cover only the Ticino and Verzasca river catchment areas, i.e., only the immediate vicinity of the Riviera. In the LU-SM2 simulations, however, we have applied the WaSiM soil moisture values over the 1 km grid where data are available. Over the rest of the domain, we use elevation-dependent values at three levels determined from averages of the WaSiM data (similar to the LU-SM setup, see Table 3). Thus, we “extrapolate” the values from the center of the domain, where the WaSiM data are available, to the rest of the Alpine region covered by the 1 km grid. The wind speed and direction from LU-SM and LU-SM2 in Fig. 13 differ significantly, although there is not as much difference in the temperatures (not shown). The onset of the valley winds sees a greater delay (by about two hours) in the morning (Fig. 13); the up-valley winds also die out about two hours too soon in the evening. Vertical profiles (not shown) indicate that these wind shift differences are present throughout the valley atmosphere and not just at the surface.

The effects of differences in soil moisture variability can also be seen by examining time series of surface fluxes. Figure 9 showed that the REF-ST surface fluxes are severely underpredicted, confirming the lack of adequate heating and the delay in the predicted onset of valley winds. Between LU-SM and LU-SM2, the differences in the heat and momentum fluxes (not shown) are much smaller but reflect the discrepancies in the valley winds predicted by LU-SM2 shown in

Fig. 13.

The results of comparisons among LU-SM, LU-SM2 and REF-ST indicate that the soil moisture outside the fine-grid (350 m) domain is crucial for accurately predicting the wind transitions. In fact, using the three-level elevation-dependent soil moisture from the 1 km grid on the 350 m grid (LU-SM3) yields results almost equivalent to LU-SM. The effect of using the WaSiM data in LU-SM is small, improving the onset of the up-valley winds by approximately half an hour; Fig. 14 shows the surface wind time series for LU-SM and LU-SM3. Note that WaSiM data are needed to obtain the three-level soil moisture values, so the LU-SM3 setup provides no practical advantage, but emphasizes the significance of the 1 km grid soil moisture initialization.

In summary, the LU-SM setup has the best possible initial soil moisture information. The simulations deteriorate in quality when we assume the large-scale ECMWF soil moisture distribution holds on the 1 km domain (REF-ST). Likewise, assuming that the local WaSiM soil moisture distribution in the Riviera Valley holds over the larger 1 km domain (LU-SM2) also yields poorer results than the three-level soil moisture used at 1 km resolution in LU-SM. This points to the need for high-resolution soil moisture measurements over a broader region (such as all of the Alps) to provide accurate input to large-eddy simulations. In our case, the sensitivity to soil moisture is highlighted in the 1 km grid, which is the first grid which can resolve the complex topography (albeit coarsely) while containing the entire valley system (i.e. the valleys surrounding the Riviera) responsible for forcing the thermal flow.

b. *Land use data*

We introduced 100 m resolution land use data for the 350 m grid level, as described previously in Section 3e. To measure the impact of the increased number of vegetation and soil classes and increased spatial variability, we performed simulations with interpolated low-resolution land use data and the original vegetation and soil types (results are denoted SM) instead of the 100 m data. The SM wind direction in Fig. 15 shows erratic behavior during the morning valley-wind transition,

and the wind speed time series shows an additional half hour delay in the up-valley winds relative to LU-SM. Differences in vertical sounding profiles are quite small except near the surface (not shown). Nevertheless, the overall results indicate that the high-resolution land use representation brings improvements.

c. Grid resolution

High grid resolution is particularly important over complex terrain like the Riviera Valley, where the terrain features that channel the flow must be well resolved. The width of the Riviera Valley floor is approximately 1.5 km. Given that the minimum well-resolved eddy for LES is $4\Delta x$, a horizontal resolution of 400 m barely resolves the valley floor. Coarse resolutions also do not represent the terrain elevation accurately. For example, the elevation of site A1 is 1123 m, 794 m, 334 m, and 263 m asl on the 9 km, 3 km, 1 km, and 350 m resolution grids, respectively. These are enormous height differences from the true elevation of 250 m asl and they greatly affect the representation of near-surface flow.

It may seem obvious that increasing resolution will improve results, but this is still debated in the literature (see e.g. Cairns and Corey 2003; Hart et al. 2004). The comparisons here show the significant improvements that can be obtained at finer resolutions when the appropriate surface data are used. Figure 16 shows comparisons of the potential temperature results from 3 km, 1 km, and 350 m horizontal resolutions from LU-SM. The plotted surface values on the coarse grids (i.e. at the first grid level) are at much higher elevation than the real valley floor; thus, the potential temperature for the 3 km and 1 km grids is too high at the surface, especially during the night. A height-correction has not been carried out, as the choice of a suitable lapse rate would have been arbitrary and would not have improved the amplitude error in the temperature curve. The wind transition predictions on the 3 km and 1 km grids are also crude in comparison to the good agreement seen at the 350 m grid level (not shown). Fig. 17 shows an example where the finer vertical resolution of the 350 m grid (see Section 3b) can capture strongly stratified layers (though

not perfectly), unlike the 3 km and 1 km grids. These near-surface inversions are influenced by shallow down-slope wind layers and are responsible for the cooling seen during the night at the valley floor. The coarse grids are not able to capture such shallow stable layers because of the poor representation of the terrain slopes and the coarse near-surface resolution (Fig. 16).

The differences between the 350 m and 150 m results (not shown) are small. This is likely due to the lateral boundary forcing and the limited domain sizes; the 150 m grid is strongly forced by the 350 m results. The increased resolution up to 350 m is, however, clearly necessary for an accurate representation of this complex flow. The general results (e.g. wind transitions) are influenced strongly by the solution on the 1 km grid, so it is important to have good soil moisture values on this grid (see Section 5a). Finer resolution allows a larger range of flow structures to be resolved, thereby better representing near-surface features (e.g. stratification), and relying less on the SFS turbulence models. At the same time, the unsatisfactory REF results (using interpolated low-resolution surface data) show that high-resolution surface data are necessary in addition to fine grid resolution.

d. *Topographic shading*

A series of simulations was performed without topographic shading for the entire set of simulations (LU-SM-NOSHADE) to investigate the influence of this modification to the radiation model. Figure 18 shows the incoming shortwave radiation with and without topographic shading, at site A1. The incoming shortwave radiation is significantly reduced around sunrise and sunset when topographic shading is included, and therefore compares better with the measurements. Figure 19 shows the spatial variation of differences in incoming shortwave radiation at 0600 UTC when topographic shading is included. The east-facing slopes are shaded while the sun is low on the horizon, resulting in nearly 300 W/m^2 less insolation. The topographic shading model does not affect the longwave radiation balance at night.

The differences in the radiation curves and flow fields are insignificant at the coarser resolu-

tions, because terrain slopes are smaller, but on the 350 m grid, surface temperatures are slightly warmer without shading (~ 0.5 - 1.0 K) during sunrise and sunset, as expected. Figure 20 shows a time series of the absolute value of differences at surface station A1 for LU-SM and LU-SM-NOSHADE. It is clear that the largest changes from topographic shading occur during sunrise and sunset. The influence of topographic shading in the comparisons of the vertical profiles is quite small.

Experiment LU-SM-NOSHADE shows increased up-slope winds along the east-facing slope of the Riviera as expected; however, differences are only on the order of 0.1 m/s, occasionally up to 0.5 m/s (not shown). Larger differences from topographic shading were observed in the idealized simulations of Colette et al. (2003), which did not include along-valley winds. Another reason why the impact of topographic shading is weaker here may be that the valley winds are forced by a pressure gradient over the entire valley wind system (i.e. from the Magadino Valley up to the Leventina Valley; see Fig. 2b). The beginning and end portions of this larger-scale valley are oriented more nearly east-west and are thus less affected by shading in the morning. In addition, the Magadino and Leventina Valleys are not entirely included in the 350 m domain. While the differences between LU-SM and LU-SM-NOSHADE are small, the improvement in the radiation curves in Fig. 18 is significant. The computational cost of adding the shading effect is negligible (Colette et al. 2003).

e. Turbulence closure

Little is known about the appropriate choice of turbulence models for LES in complex terrain. One measure of the influence of the turbulence model is the effect of turning the turbulence model on or off, as seen in Fig. 21 for LU-SM and LU-SM-NOTURB. The “no turbulence” simulations clearly do not perform as well as LU-SM. The surface wind predictions have significant differences; for example, the surface winds show more oscillations, as expected for a simulation with less dissipation. The difference in the results is limited, however, to the near-surface region, because the

SFS stress contribution is large only in the lowest 500 m, as shown in Figs. 11-12. This is due to the strong stable stratification in the valley atmosphere, with only a shallow mixed layer at the surface (Fig. 8). Accordingly, vertical profiles from LU-SM and LU-SM-NOTURB only show differences in the near-surface region (not shown). Intermittent turbulence may be important in stable layers above, but this is hard to capture with current turbulence models (Cederwall 2001). All of the simulations also include fourth-order computational mixing, which acts like a hyper-viscosity term and may dominate the turbulence model effect at 350 m resolution. Numerical errors from finite-difference schemes also contribute to the dissipation of energy from large to small scales.

Simulations are also performed using the dynamic reconstruction model (DRM) of Chow et al. (2005) (LU-SM-DRM). The differences in the TKE-1.5 and DRM predictions of the temperature and winds are not large, so they are not shown here. Details of the models and comparisons are given in Chow (2004). The most noticeable change is in the prediction of momentum fluxes. Figure 22 shows vertical profiles of time-averaged resolved and SFS stresses in the vw plane from LU-SM-DRM. Compared to Fig. 12, the DRM results give a significantly larger contribution from the SFS terms. This is consistent with the findings in Chow et al. (2005) where the SFS stresses using DRM were larger (than those from an eddy-viscosity model used alone) due to the resolved subfilter-scale (RSFS) contribution, and hence gave better comparisons to stresses extracted from higher-resolution simulations. Here, the stress is also larger higher up in the valley atmosphere because the DRM is not as easily damped by stratification when the RSFS stress is included.

The simulation results show relative insensitivity to the turbulence model because differences are confined to the near-surface region. (In contrast, the sensitivity to soil moisture initialization was high, where differences extended throughout the valley atmosphere and affected wind transitions, as seen, for example, in Figs. 5-8.) The limited influence of the turbulence model is due to the role of the strong stratification and also the strong lateral boundary forcing. The lateral boundary conditions are time dependent, but are only updated hourly. Intermediate values are linearly interpolated. Simulations of flow over Askervein Hill (Chow and Street 2004) showed that realistic

turbulent inflow conditions were necessary for satisfactory predictions of wind speed over the hill. The lateral forcing in the Riviera is not fully turbulent because of the linear time interpolation, so the turbulence must develop as the flow progresses through the domain and is influenced by the complex topography. Small-scale turbulent motions are present in the simulations, but the afternoon winds are quite strong, yielding a relatively short effective residence time of air parcels in the valley when compared to the 30-hour simulation time. Thus, small differences that arise due to different turbulence models (or topographic shading and other parameterizations) do not have time to manifest themselves especially when along-valley winds are strong.

Figure 23 shows that differences do occur on shorter time scales, comparing results from one-hour simulations using identical initial and boundary conditions but different turbulence models (the TKE-1.5 and the DRM). It is clear that the shape of the up-valley flow contours is different, and hence that the effect of the turbulence closure is not completely negligible, even though the performance of the models is difficult to quantitatively evaluate because of the lack of high-resolution observation data. Simulations over the entire day are more strongly influenced by lateral boundary conditions and surface characteristics, but the finer details are affected by the turbulence model.

6. Summary and conclusions

We have shown that ARPS can accurately reproduce the valley wind patterns observed under convective conditions in complex terrain. Comparisons to surface station and radiosonde measurements from the MAP-Riviera project field campaign of 1999 gave rmse values of less than 1 K for potential temperature and of about 2 m/s for wind speed. This success required careful initialization with high-resolution land use and soil moisture datasets, among other considerations. In contrast, increasing resolution without using high-resolution surface datasets did not yield satisfactory results. It was found that even with strong local thermal forcing, the onset and magnitude of the valley wind transitions are highly sensitive to surface fluxes in areas which are well outside the high-resolution domain. These processes directly influence the flow structure in the high-resolution

domain via its lateral boundary conditions, but are inadequately resolved on the coarser grid of the previous nesting level. The three-dimensional structure and evolution of the valley boundary layer is investigated in detail in Part II (Weigel et al. 2005).

Our findings can be summarized as follows:

(i) Increased grid resolution provides improved numerical simulations, but only when surface and soil model fields are properly initialized. While 3 km horizontal spacing is often considered to be high resolution, it is not until we reach 350 m resolution that the wind transitions and vertical structure of the atmosphere become very well represented in a narrow valley. Even higher grid resolution will allow the representation of finer-scale motions and may improve the ability of SGS turbulence models to contribute appropriately under stable stratification.

(ii) High-resolution soil moisture data proved to be necessary to obtain the most accurate predictions of wind transitions and surface fluxes. Improved soil moisture data (three-level elevation dependent values, motivated by WaSiM data) were crucial at the 1 km grid level, where the entire Riviera Valley is included in the domain and valley winds are generated over the whole valley network. High-resolution initial soil moisture data (100 m, obtained from the hydrologic model WaSiM), gave further improvement at the 350 m grid. All in all, the distribution of soil moisture was one of the most sensitive parameters in our simulations. The 100 m land use data provided detailed local land coverage and also improved simulation results, as did initializing the soil temperature with an offset from the air temperature, but the sensitivity to these modifications was not as large as for the soil moisture initialization.

(iii) Topographic shading improved the radiation curves measured at the valley floor and along the slopes, with the largest differences occurring during sunrise and sunset. The influence of topographic shading was only significant at the 350 m and finer grids where the steep topography is well resolved. The overall impact of topographic shading on the flow dynamics is small (see Fig. 18) because the fine-resolution flow is driven through grid nesting by the coarser resolution grid which is not sensitive to the shading.

(iv) The effect of different turbulence models in the Riviera Valley is unclear. Simulations without a turbulence model performed poorly in comparisons with surface observations. Results with the dynamic reconstruction approach, however, did not differ appreciably over the simulation period from the standard TKE-1.5 closure, perhaps because the turbulent stresses were only significant in the lowest 500 m near the surface (due to strong stratification) and because of strong lateral boundary forcing. There are visible effects on near-surface eddy structures but quantitative verification data are not available.

(v) The lateral boundary forcing is largely responsible for driving the flow transitions at the 350 m and 150 m grids. Thus the valley wind transitions are strongly influenced by the 1 km grid where the entire Riviera Valley is included in the domain. Unfortunately at 1 km resolution, the topography is not well resolved and surface data are sparser so errors are larger. The strong lateral boundary forcing limits our ability to fully evaluate the sensitivity of the topographic shading and turbulence closure models; the grid nesting effectively constrains the influence of these model components to the finest grids because of poor resolution on the larger grids.

The sensitivity to surface conditions points to a need for better surface characterization data. Extensive field campaigns and remote sensing developments are needed to obtain the necessary input data for forecast models. Accurate soil moisture data at 1 km resolution, for example, was found to be necessary for the success of the Riviera Valley flow simulations, but most field campaigns include at best a handful of soil moisture measurement locations. The design of such field campaigns could be greatly improved by examining model results like those obtained here for the Riviera Valley. Much research is also needed to construct radiation models that include the influence of neighboring terrain on local radiative heat fluxes that are important in steep terrain. Grid nesting techniques at the lateral boundaries also need further exploration. The transmission of turbulent fluctuations from the coarse to the fine grid at the lateral boundaries is currently severely limited by the grid resolution and the frequency at which lateral boundary condition data are available. More frequent boundary condition updates and two-way nesting techniques should

be investigated.

Acknowledgments Many thanks go to Massimiliano Zappa and Karsten Jasper for providing soil moisture initialization data from WaSiM-ETH, and to Hans Volkert for providing the 100 m topography data. We gratefully acknowledge the support of a National Defense Science and Engineering Graduate fellowship [FKC], National Science Foundation Grants ATM-0073395 (Physical Meteorology Program: W.A. Cooper, Program Director) [FKC and RLS], ATM-0129892, ATM-0331594, and EEC-0313747 [MX], and Swiss National Science Foundation Grants #20-68320.01 and #20-100013 [APW]. Acknowledgment is also made to the National Center for Atmospheric Research, which is sponsored by NSF, for the computing time used in this research. Part of this work was performed under the auspices of the U.S. Department of Energy by the University of California, Lawrence Livermore National Laboratory under Contract W-7405-Eng-48.

References

- Banta, R. M. and P. T. Gannon, 1995: Influence of soil moisture on simulations of katabatic flow. *Theor. Appl. Climatol.*, **52**, 85 – 94.
- Benoit, R., C. Schär, P. Binder, S. Chamberland, H. C. Davies, M. Desgagne, C. Girard, C. Keil, N. Kouwen, D. Luthi, D. Maric, E. Muller, P. Pellerin, J. Schmidli, F. Schubiger, C. Schwierz, M. Sprenger, A. Walser, S. Willemsse, W. Yu, and E. Zala, 2002: The real-time ultra-fine-scale forecast support during the Special Observing Period of the MAP. *Bull. Amer. Met. Soc.*, **83**, 85 – 109.
- Bougeault, P., P. Binder, A. Buzzi, R. Dirks, R. Houze, J. Kuettner, R. B. Smith, R. Steinacker, and H. Volkert, 2001: The MAP Special Observing Period. *Bull. Amer. Met. Soc.*, **82**, 433 – 462.
- Cairns, M. M. and J. Corey, 2003: Mesoscale model simulations of high-wind events in the complex terrain of western Nevada. *Wea. Forecast.*, **18**, 249–263.

- Cederwall, R. T., 2001: *Large-eddy simulation of the evolving stable boundary layer over flat terrain*. Ph.D. dissertation, Stanford University.
- Chen, F., T. T. Warner, and K. Manning, 2001: Sensitivity of orographic moist convection to landscape variability. A study of the Buffalo Creek, Colorado, flash flood case of 1996. *J. Atmos. Sci.*, **58**, 3204 – 3223.
- Chen, Y., F. L. Ludwig, and R. L. Street, 2004: Stably stratified flows near a notched transverse ridge across the Salt Lake Valley. *J. Appl. Meteor.*, **43**, 1308–1328.
- Chow, F. K., 2004: *Subfilter-scale turbulence modeling for large-eddy simulation of the atmospheric boundary layer over complex terrain*. Ph.D. dissertation, Stanford University.
- Chow, F. K. and R. L. Street, 2004: Evaluation of turbulence models for large-eddy simulations of flow over Askervein hill. Paper 7.11. *Amer. Meteor. Soc., 16th Symp. Bound. Layers Turb.*
- Chow, F. K., R. L. Street, M. Xue, and J. H. Ferziger, 2005: Explicit filtering and reconstruction turbulence modeling for large-eddy simulation of neutral boundary layer flow. *J. Atmos. Sci.*, **in press**.
- Colette, A., F. K. Chow, and R. L. Street, 2003: A numerical study of inversion-layer breakup and the effects of topographic shading in idealized valleys. *J. Appl. Meteor.*, **42**, 1255 – 1272.
- De Wekker, S., 2002: *Structure and morphology of the convective boundary layer in mountainous terrain*. Ph.D. dissertation, University of British Columbia.
- De Wekker, S., D. G. Steyn, J. D. Fast, M. W. Rotach, and S. Zhong, 2005: The performance of RAMS in representing the convective boundary layer structure in a very steep valley. *Environ. Fluid Mech.*, **5**, 35–62.
- Deardorff, J. W., 1980: Stratocumulus-capped mixed layers derived from a 3-dimensional model. *Bound.-Layer Meteor.*, **18**, 495 – 527.

- Eastman, J. L., R. A. Pielke, and D. J. McDonald, 1998: Calibration of soil moisture for large-eddy simulations over the FIFE area. *J. Atmos. Sci.*, **55**, 1131–1140.
- Germano, M., 1996: A statistical formulation of the dynamic model. *Phys. Fluids*, **8**, 565 – 570.
- Gohm, A., G. Zängl, and G. J. Mayr, 2004: South Foehn in the Wipp Valley on 24 October 1999 (MAP IOP 10): Verification of high-resolution numerical simulations with observations. *Mon. Wea. Rev.*, **132**, 78 – 102.
- Grell, G. A., S. Emeis, W. R. Stockwell, T. Schoenemeyer, R. Forkel, J. Michalakes, R. Knoche, and W. Seidl, 2000: Application of a multiscale, coupled MM5/chemistry model to the complex terrain of the VOTALP valley campaign. *Atmos. Environ.*, **34**, 1435 – 1453.
- Grønås, S. and A. D. Sandvik, 1999: Numerical simulations of local winds over steep orography in the storm over north Norway on October 12, 1996. *J. Geophys. Res.*, **104**, 9107–9120.
- Hanna, S. R. and R. X. Yang, 2001: Evaluations of mesoscale models' simulations of near-surface winds, temperature gradients, and mixing depths. *J. Appl. Meteor.*, **40**, 1095 – 1104.
- Hart, K. A., W. J. Steenburgh, D. J. Onton, and A. J. Siffert, 2004: An evaluation of mesoscale-model-based model output statistics (MOS) during the 2002 Olympic and Paralympic Winter Games. *Wea. Forecast.*, **19**, 200–218.
- Jacobson, M. Z., 2001: GATOR-GCMM - 2. A study of daytime and nighttime ozone layers aloft, ozone in national parks, and weather during the SARMAP field campaign. *J. Geophys. Res.*, **106**, 5403 – 5420.
- Jasper, K., 2001: *Hydrological modelling of Alpine river catchments using output variables from atmospheric models*. Ph.D. dissertation, ETH No. 14385, Swiss Federal Institute of Technology, Zurich.

- Kravchenko, A. G., P. Moin, and R. Moser, 1996: Zonal embedded grids for numerical simulations of wall-bounded turbulent flows. *J. Comput. Phys.*, **127**, 412–423.
- Lilly, D. K., 1962: On the numerical simulation of buoyant convection. *Tellus*, **14**, 148–172.
- Lu, R. and R. P. Turco, 1995: Air pollutant transport in a coastal environment – II. three-dimensional simulations over Los Angeles basin. *Atmos. Environ.*, **29**, 1499 – 1518.
- Mahrer, Y., 1984: An improved numerical approximation of the horizontal gradients in a terrain-following coordinate system. *Mon. Wea. Rev.*, **112**, 918 – 922.
- Matzinger, N., M. Andretta, E. V. Gorsel, R. Vogt, A. Ohmura, and M. W. Rotach, 2003: Surface radiation budget in an Alpine valley. *Quart. J. Roy. Meteor. Soc.*, **129**, 877 – 895.
- Moeng, C.-H., 1984: A large-eddy-simulation model for the study of planetary boundary-layer turbulence. *J. Atmos. Sci.*, **41**, 2052–2062.
- Ookouchi, Y., M. Segal, R. C. Kessler, and R. A. Pielke, 1984: Evaluation of soil moisture effects on the generation and modification of mesoscale circulations. *Mon. Wea. Rev.*, **112**, 2281 – 2292.
- Pope, S. B., 2000: *Turbulent flows*. Cambridge University Press, Cambridge, UK, 770 pp.
- Poulos, G., 1999: *The interaction of katabatic winds and mountain waves*. Ph.D. dissertation, Colorado State University.
- Revell, M. J., D. Purnell, and M. K. Lauren, 1996: Requirements for large-eddy simulation of surface wind gusts in a mountain valley. *Bound.-Layer Meteor.*, **80**, 333–353.
- Rotach, M. W., P. Calanca, G. Graziani, J. Gurtz, D. G. Steyn, R. Vogt, M. Andretta, A. Christen, S. Cieslik, R. Conolly, S. De Wekker, S. Galmarini, E. N. Kadygrov, V. Kadygrov, E. Miller, B. Neininger, M. Rucker, E. Van Gorsel, H. Weber, A. Weiss, and M. Zappa, 2004: Turbulence structure and exchange processes in an Alpine valley: The Riviera Project. *Bull. Amer. Met. Soc.*, **85**, 1367–1385.

- Smagorinsky, J., 1963: General circulation experiments with the primitive equations. *Mon. Wea. Rev.*, **91**, 99–152.
- Van Gorsel, E., A. Christen, C. Feigenwinter, E. Parlow, and R. Vogt, 2003: Daytime turbulence statistics above a steep forested slope. *Bound.-Layer Meteor.*, **109**, 311 – 329.
- Volkert, H., 1990: An Alpine orography resolving major valleys and massifs. *Meteor. Atmos. Phys.*, **43**, 231 – 234.
- Warner, T. T., R. A. Peterson, and R. E. Treadon, 1997: A tutorial on lateral boundary conditions as a basic and potentially serious limitation to regional numerical weather prediction. *Bull. Amer. Met. Soc.*, **78**, 2599 – 2617.
- Weigel, A. P., F. K. Chow, M. W. Rotach, R. L. Street, and M. Xue, 2005: High-resolution large-eddy simulations of flow in a steep Alpine valley. Part II: Flow structure and heat budgets. *J. Appl. Meteor.*, **submitted for publication**.
- Weigel, A. P. and M. W. Rotach, 2004: Flow structure and turbulence characteristics of the daytime atmosphere in a steep and narrow Alpine valley. *Quart. J. Roy. Meteor. Soc.*, **130**, 2605–2628.
- Whiteman, C. D., 2000: *Mountain meteorology: fundamentals and applications*. Oxford University Press, New York, 355 pp.
- Whiteman, C. D., B. Pospichal, S. Eisenbach, P. Weihs, C. B. Clements, R. Steinacker, E. Mursch-Radlgruber, and M. Dorninger, 2004: Inversion breakup in small Rocky Mountain and Alpine basins. *J. Appl. Meteor.*, **43**, 1069–1082.
- Wong, V. C. and D. K. Lilly, 1994: A comparison of two dynamic subgrid closure methods for turbulent thermal-convection. *Phys. Fluids*, **6**, 1016 – 1023.
- Wyngaard, J. C., 2004: Toward numerical modeling in the “Terra Incognita”. *J. Atmos. Sci.*, **61**, 1816–1826.

- Xue, M., K. K. Droegemeier, and V. Wong, 2000: The Advanced Regional Prediction System (ARPS): A multi-scale nonhydrostatic atmospheric simulation and prediction model. Part I: Model dynamics and verification. *Meteor. Atmos. Phys.*, **75**, 161–193.
- Xue, M., K. K. Droegemeier, V. Wong, A. Shapiro, and K. Brewster, 1995: *ARPS Version 4.0 User's Guide*. Center for Analysis and Prediction of Storms, University of Oklahoma, Norman, OK.
- Xue, M., K. K. Droegemeier, V. Wong, A. Shapiro, K. Brewster, F. Carr, D. Weber, Y. Liu, and D. Wang, 2001: The Advanced Regional Prediction System (ARPS): A multi-scale nonhydrostatic atmospheric simulation and prediction tool. Part II: Model physics and applications. *Meteor. Atmos. Phys.*, **76**, 143–165.
- Xue, M., D. Wang, J. Gao, K. Brewster, and K. K. Droegemeier, 2003: The Advanced Regional Prediction System (ARPS), storm-scale numerical weather prediction and data assimilation. *Meteorology and Atmospheric Physics*, **82**, 139 – 170.
- Zängl, G., B. Chimani, and C. Haberli, 2004: Numerical simulations of the Foehn in the Rhine Valley on 24 October 1999 (MAP IOP 10). *Mon. Wea. Rev.*, **132**, 368 – 389.
- Zappa, M. and J. Gurtz, 2003: Simulation of soil moisture and evapotranspiration in a soil profile during the 1999 MAP-Riviera campaign. *Hydrol. Earth Sys. Sci.*, **7**, 903–919.
- Zhong, S. Y. and J. Fast, 2003: An evaluation of the MM5, RAMS, and Meso-Eta models at subkilometer resolution using VTMX field campaign data in the Salt Lake Valley. *Mon. Wea. Rev.*, **131**, 1301 – 1322.

List of Tables

- 1 Riviera Valley simulation configurations. ECMWF and WaSiM soil moisture data have 0.5 degree (~ 60 km) and 100 m resolution, respectively. The coarse USGS land use data is at 30 s (~ 1 km) spacing as opposed to the 100 m GEOSTAT data. REF is the reference run using low-resolution surface data. REF-ST initializes soil temperature (ST) as an offset from the air temperature as opposed to using interpolation from ECMWF values. The LU-SM run name indicates the use of high-resolution land use (LU) and high-resolution soil moisture (SM) data, in addition to the soil temperature offset from REF-ST. Other run names are constructed similarly and represent variations from the LU-SM configuration. See text for details. 38
- 2 Nested grid configurations, with dimensions and time step sizes. In the vertical direction, the minimum grid spacing is Δz_{min} at the surface, and the averaging spacing is Δz_{avg} . Δt denotes the large time step and $\Delta \tau$ the small time step, selected such that $2\Delta t = n\Delta \tau$, where $n = 1, 2, \dots$ 39
- 3 Typical soil moisture values ($m^3 m^{-3}$) for each dataset in the surface and deep layers. All have close to zero soil moisture at the rocky outcroppings and in urban areas. The surface layer does not vary as much as the deep layer so the differences between the valley and slope are not given. The 3-level data are constant in each elevation range. 40
- 4 Surface station locations. 41

5	<p>Root-mean-square errors (rmse) and mean errors (bias) for potential temperature, wind speed, and wind direction, for simulations compared to observations at site C (western slope) at 5 m agl, at site A1 using the average of 15.9 and 28 m values, and at sites B, E1, and E2 on the eastern slope using data from measurements at 22 m , 12.7 m, and 22.7, respectively; see Table 4. Note that the measurements at 5 m agl for site C do not agree as well with the simulations because of the low measurement height, where the influence from the vegetation canopy is large. . . .</p>	42
6	<p>Root-mean-square errors and mean errors (bias) for potential temperature, wind speed, wind direction, and specific humidity, for each radiosonde launch for LUSM. The summary of all radiosonde launches is given in the column labeled “All”; comparisons to the REF and REF-ST results are also shown. Wind observation data were not available (NA) for 0600 UTC. ARPS data were taken from output at nearest half hour. . . .</p>	43

Table 1: Riviera Valley simulation configurations. ECMWF and WaSiM soil moisture data have 0.5 degree (~ 60 km) and 100 m resolution, respectively. The coarse USGS land use data is at 30 s (~ 1 km) spacing as opposed to the 100 m GEOSTAT data. REF is the reference run using low-resolution surface data. REF-ST initializes soil temperature (ST) as an offset from the air temperature as opposed to using interpolation from ECMWF values. The LU-SM run name indicates the use of high-resolution land use (LU) and high-resolution soil moisture (SM) data, in addition to the soil temperature offset from REF-ST. Other run names are constructed similarly and represent variations from the LU-SM configuration. See text for details.

Run name	Soil moisture		Soil temp.	Land use	Topo.	Turbulence
	1 km grid	350 m grid	350 m grid	350 m grid	shading	350 m grid
REF	ECMWF	ECMWF	ECMWF	1 km	Yes	TKE-1.5
REF-ST	ECMWF	ECMWF	offset	1 km	Yes	TKE-1.5
LU-SM	3-level	WaSiM	offset	100 m	Yes	TKE-1.5
LU-SM2	WaSiM/3-level	WaSiM	offset	100 m	Yes	TKE-1.5
LU-SM3	3-level	3-level	offset	100 m	Yes	TKE-1.5
SM	3-level	WaSiM	offset	1 km	Yes	TKE-1.5
LU-SM-NOSHADE	3-level	WaSiM	offset	100 m	No	TKE-1.5
LU-SM-NOTURB	3-level	WaSiM	offset	100 m	Yes	None
LU-SM-DRM	3-level	WaSiM	offset	100 m	Yes	DRM

Table 2: Nested grid configurations, with dimensions and time step sizes. In the vertical direction, the minimum grid spacing is Δz_{min} at the surface, and the averaging spacing is Δz_{avg} . Δt denotes the large time step and $\Delta \tau$ the small time step, selected such that $2\Delta t = n\Delta \tau$, where $n = 1, 2, \dots$

Grid size (nx, ny, nz)	$\Delta x, \Delta y$	Δz_{min}	Δz_{avg}	Domain height	$\Delta t / \Delta \tau$
$103 \times 103 \times 53$	9 km	50 m	500 m	25 km	10 s / 10 s
$103 \times 103 \times 53$	3 km	50 m	500 m	25 km	2 s / 4 s
$99 \times 99 \times 63$	1 km	50 m	400 m	24 km	1 s / 1 s
$83 \times 83 \times 63$	350 m	30 m	350 m	21 km	1 s / 0.2 s
$67 \times 99 \times 83$	150 m	20 m	200 m	16 km	0.5 s / 0.05 s

Table 3: Typical soil moisture values (m^3m^{-3}) for each dataset in the surface and deep layers. All have close to zero soil moisture at the rocky outcroppings and in urban areas. The surface layer does not vary as much as the deep layer so the differences between the valley and slope are not given. The 3-level data are constant in each elevation range.

	Surface (0.01 m)	Deep (1.0 m)	
		Valley floor (< 500 m asl)	Slopes (500 - 2200 m asl)
ECMWF	0.35	0.37	0.37
WaSiM	0.32	0.25	0.10
3-level	same as deep	0.28	0.18

Table 4: Surface station locations, shown in Fig. 2b.

Site	Name	Location	Elevation asl	Measurement height agl
A1	Bosco di Sotto	Valley floor (46.265 N, 9.012 E)	250 m	15.9, 28 m
B	Rored	Eastern slope (46.263 N, 9.031 E)	760 m	22, 28 m
C	Pian Perdascio	Western slope (46.238 N, 9.005 E)	340 m	5 m
E1	Roasco	Eastern slope (46.267 N, 9.037 E)	1060 m	2,12.7 m
E2	Monte Nuovo	Eastern slope (46.271 N, 9.036 E)	1030 m	16.8,22.7 m

Table 5: Root-mean-square errors (rmse) and mean errors (bias) for potential temperature, wind speed, and wind direction, for simulations compared to observations at site C (western slope) at 5 m agl, at site A1 using the average of 15.9 and 28 m values, and at sites B, E1, and E2 on the eastern slope using data from measurements at 22 m , 12.7 m, and 22.7, respectively; see Table 4. Note that the measurements at 5 m agl for site C do not agree as well with the simulations because of the low measurement height, where the influence from the vegetation canopy is large.

Site	Run	θ (K)		U (m/s)		ϕ (deg)	
		rmse	bias	rmse	bias	rmse	bias
A1	REF	3.20	-3.04	1.47	-0.53	86.42	-1.50
	REF-ST	1.60	-1.39	1.25	-0.26	70.92	-9.33
	LU-SM	0.69	-0.41	1.28	0.57	63.21	-11.05
B	REF	1.00	-0.05	0.70	0.14	93.24	-10.92
	REF-ST	0.89	0.06	0.85	0.27	77.06	-9.63
	LU-SM	1.08	0.75	1.24	0.77	88.21	-27.19
C	REF	4.88	4.40	0.68	0.16	69.97	-35.79
	REF-ST	5.03	4.57	0.53	0.04	65.26	-23.42
	LU-SM	5.44	5.20	0.79	0.47	69.57	-3.17
E1	REF	1.04	-0.38	1.56	-0.99	56.17	14.95
	REF-ST	0.96	-0.37	1.53	-1.01	57.65	11.11
	LU-SM	0.60	0.12	1.44	-0.61	53.14	11.98
E2	REF	1.29	-1.17	0.97	0.22	57.72	-9.94
	REF-ST	1.32	-1.22	0.84	-0.25	61.79	-14.93
	LU-SM	0.81	-0.74	0.85	0.16	54.52	-11.83

Table 6: Root-mean-square errors and mean errors (bias) for potential temperature, wind speed, wind direction, and specific humidity, for each radiosonde launch for LU-SM. The summary of all radiosonde launches is given in the column labeled “All”; comparisons to the REF and REF-ST results are also shown. Wind observation data were not available (NA) for 0600 UTC. ARPS data were taken from output at nearest half hour.

Site	Run	θ (K)		U (m/s)		ϕ (deg)		q (g/kg)	
		rmse	bias	rmse	bias	rmse	bias	rmse	bias
LU-SM	0001	1.17	0.21	1.94	-0.05	38.00	-16.33	1.02	0.28
	0600	1.26	0.48	NA	NA	NA	NA	1.16	-0.35
	0739	0.82	-0.38	2.35	0.93	65.88	-7.10	1.15	-0.15
	0915	0.66	-0.34	1.99	-0.38	31.74	-11.30	0.93	-0.79
	1208	1.06	-0.80	1.75	-0.41	24.26	-4.27	1.24	0.04
	1508	0.99	-0.77	1.81	-0.09	61.29	-8.71	1.21	0.08
	1800	0.56	0.00	2.77	-0.90	54.09	16.13	1.33	-0.06
	2118	0.75	-0.15	2.29	0.20	23.96	-10.36	1.26	-0.95
LU-SM	All	0.94	-0.22	2.04	-0.12	45.73	-5.99	1.17	-0.24
REF	All	1.43	-0.73	2.29	-0.35	55.47	3.96	1.45	-0.75
REF-ST	All	1.14	-0.52	2.26	-0.34	44.80	-3.17	1.27	-0.56

List of Figures

1	Location of the Riviera Valley in the Alps, with elevation contours (m asl). Box outlines the 1 km grid for the Riviera region, shown in detail in Fig. 2a.	47
2	Riviera Valley elevation contours (m asl) for (a) the 1 km grid and (b) the 350 m grid with the 150 m grid shown within. Locations of surface stations (defined in Table 4) and vertical cross-section are also shown.	48
3	Contours of WaSiM soil moisture initialization (m^3/m^3 , shaded) at (a) surface and (b) deep soil levels at 350 m resolution. Topography contours are shown at 250 m intervals.	49
4	Surface potential temperature time series at Bosco di Sotto (site A1). —●— Observations; —○— LU-SM; —×— REF-ST; —□— REF	50
5	Surface data time series comparisons at Bosco di Sotto for wind speed and direction. 51	
6	Surface data time series comparisons at Pian Perdascio (site C, on western slope) for (a) wind speed and (b) wind direction. —●— Observations at 5 m agl; —○— LU-SM; —×— REF-ST	52
7	Surface data time series comparisons at Monte Nuovo for wind speed and direction. 53	
8	0739, 0915, and 1208 UTC radiosonde observations compared to simulations at Bosco di Sotto (site A1) of potential temperature, wind speed, wind direction, and specific humidity on 25 August, 1999. Note that ϕ is equivalent to $\phi + 360$ Observations; — LU-SM; ---- REF-ST	54
8	Continued for 1508, 1800, and 2118 UTC.	55
9	Time series of kinematic sensible heat ($\overline{w\theta}$) flux at (a) site A1 (valley floor) and (b) site B (eastern slope). ● Observations; —○— LU-SM; —×— REF-ST.	56
10	Radiation budget components from LU-SM compared to observations at site A1.	57

11	Vertical cross-sections of (a) resolved vw and (b) SFS τ_{23} stress (m^2/s^2) perpendicular to valley axis at site A1 for LU-SM. Time averaged between 1300 and 1500 UTC at 300 s intervals. The black contour line marks the zero contour.	58
12	Vertical profile of resolved, subfilter-scale, and total stress for vw located on valley floor for LU-SM. Time averaged between 1300 and 1500 UTC at 300 s intervals.	59
13	Surface wind speed and direction at Bosco di Sotto (site A1) using different soil moisture initializations. —●— Observations; —○— LU-SM; —×— LU-SM2	60
14	Surface wind speed at site A1 using different soil moisture initializations. —●— Observations; —○— LU-SM; —×— LU-SM3	61
15	Surface wind speed and direction at Bosco di Sotto (site A1) using different land use data. —●— Observations; —○— LU-SM; —×— SM	62
16	Surface potential temperature at site A1 at various grid resolutions for LU-SM. —●— Observations; —□— 3 km; —×— 1 km; —○— 350 m	63
17	Close-up of potential temperature soundings at 1800 UTC and various grid resolutions for LU-SM. •••• Observations; —— 3 km; ---- 1 km; ——— 350 m.	64
18	Incoming solar radiation, with and without topographic shading, at site A1. * Observations; ——— LU-SM; ---- LU-SM-NOSHADE	65
19	Difference in shortwave incoming radiation with/without shading.	66
20	Time series of the absolute difference between LU-SM and LU-SM-NOSHADE surface variables at site A1 for (a) potential temperature, (b) wind speed, and (c) wind direction.	67
21	Surface wind time series comparisons with and without a turbulence model at Bosco di Sotto (site A1) for (a) wind speed and (b) wind direction. —●— Observations; —○— LU-SM; —×— LU-SM-NOTURB	68

22	Vertical profile of resolved, subfilter-scale, and total stress for vw at the valley floor for LU-SM-DRM (using the DRM turbulence closure). Time averaged between 1300 and 1500 UTC at 300 s intervals.	69
23	Cross-valley winds (vectors) and along-valley winds (m/s, shaded) at 1300 UTC from the 350 m grid for (a) LU-SM with TKE-1.5 and (b) LU-SM-DRM with the DRM turbulence closure. Simulations start at 1200 UTC using identical initial and boundary conditions. Cross-valley distance measured along line shown in Fig. 2b. The zero contour line is shown in bold.	70

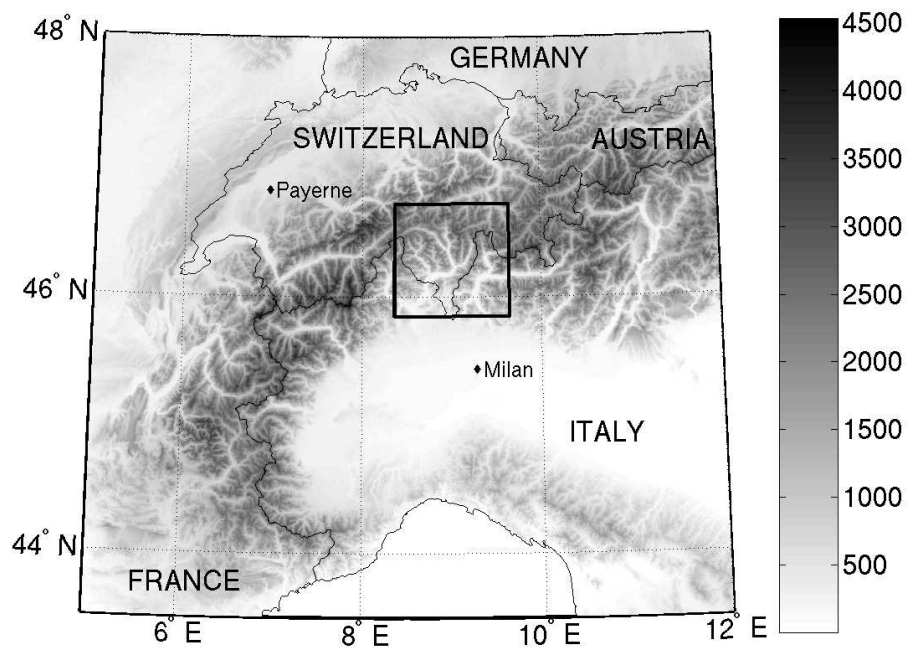
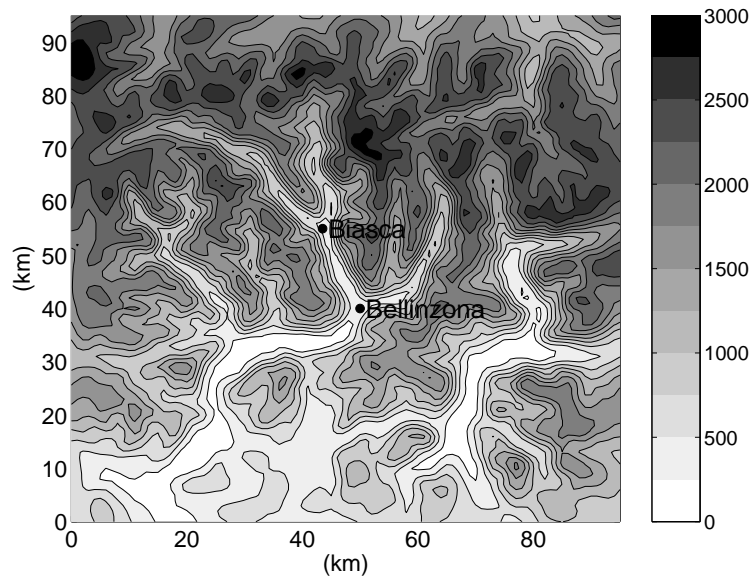
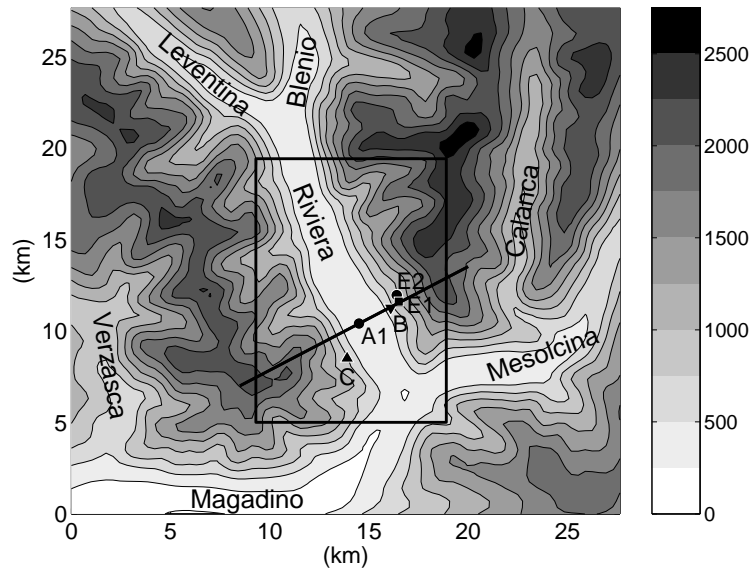


Figure 1: Location of the Riviera Valley in the Alps, with elevation contours (m asl). Box outlines the 1 km grid for the Riviera region, shown in detail in Fig. 2a.

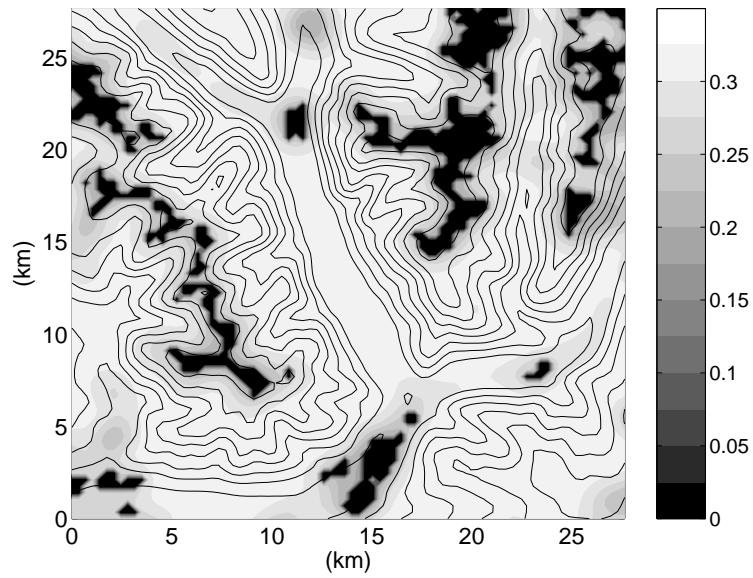


(a)

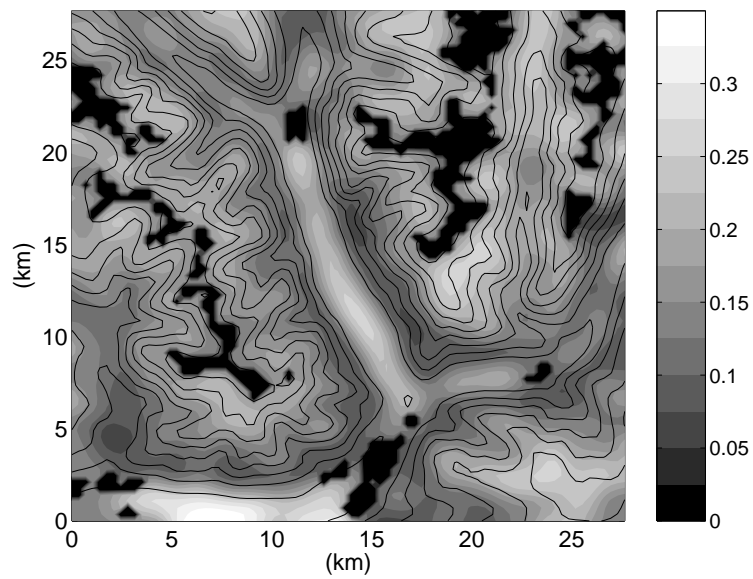


(b)

Figure 2: Riviera Valley elevation contours (m asl) for (a) the 1 km grid and (b) the 350 m grid with the 150 m grid shown within. Locations of surface stations (defined in Table 4) and vertical cross-section are also shown.



(a)



(b)

Figure 3: Contours of WaSiM soil moisture initialization (m^3/m^3 , shaded) at (a) surface and (b) deep soil levels at 350 m resolution. Topography contours are shown at 250 m intervals.

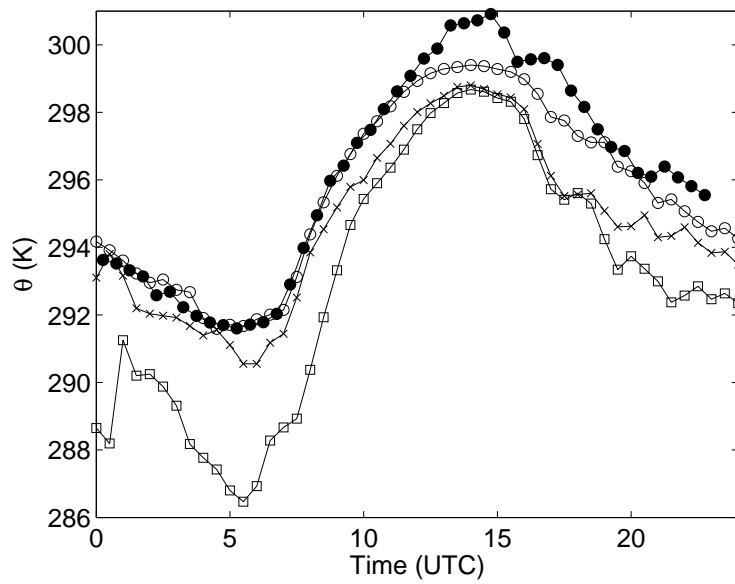
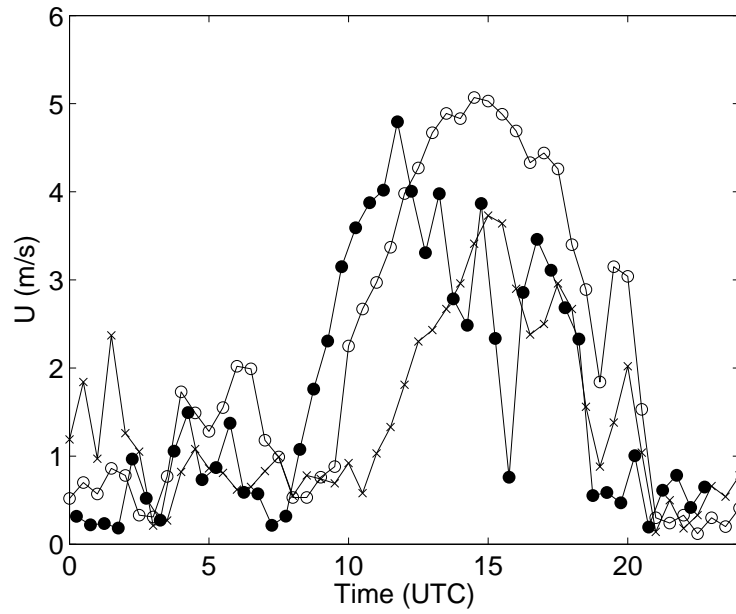
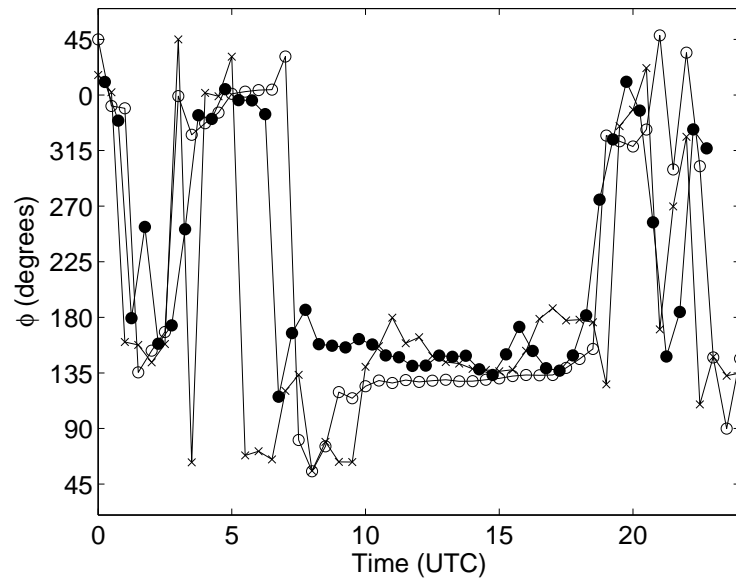


Figure 4: Surface potential temperature time series at Bosco di Sotto (site A1). —●— Observations; —○— LU-SM; —×— REF-ST; —□— REF

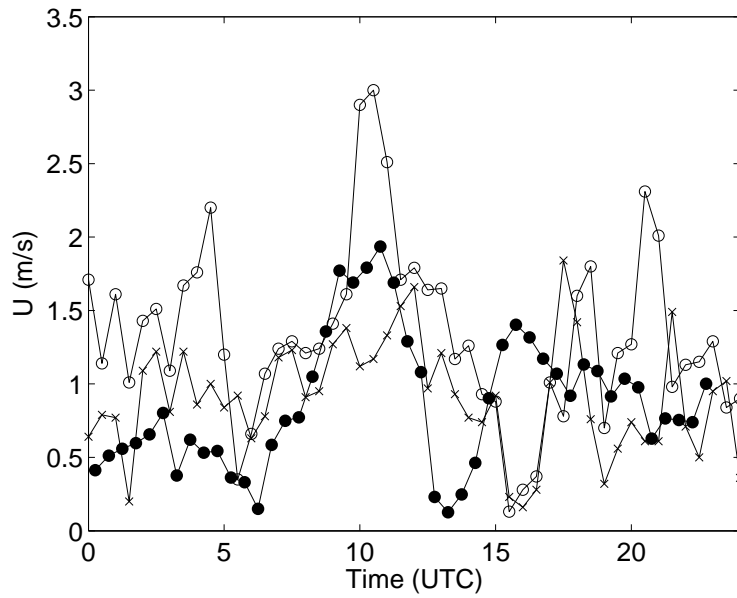


(a)

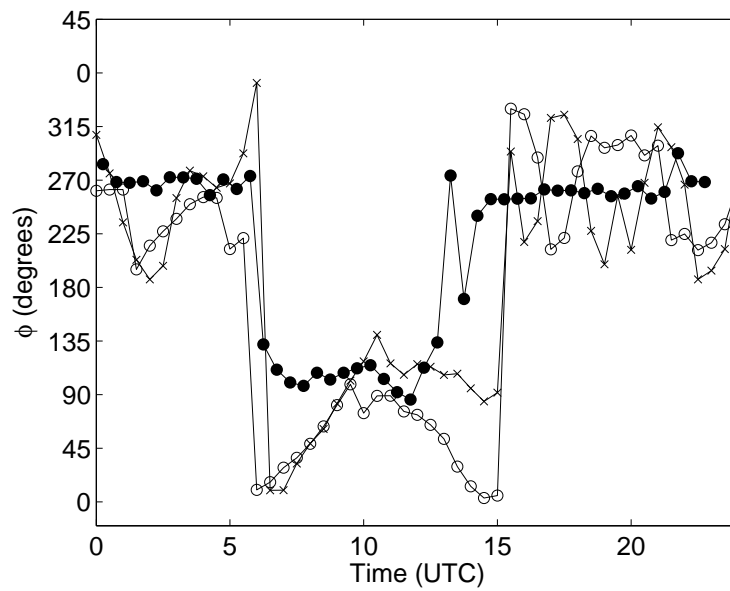


(b)

Figure 5: Surface data time series comparisons at Bosco di Sotto (site A1, valley floor) for (a) wind speed and (b) wind direction. —●— Observations (averaged from 15.9 and 28 m agl); —○— LU-SM; —×— REF-ST

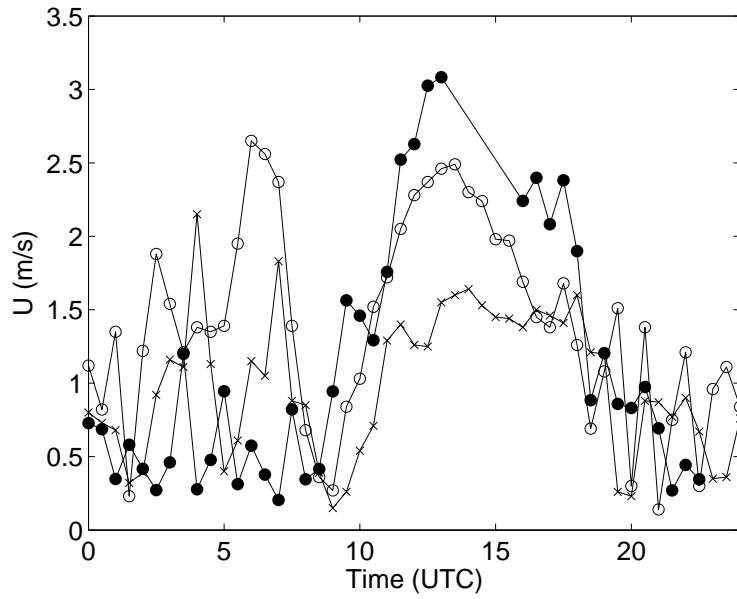


(a)

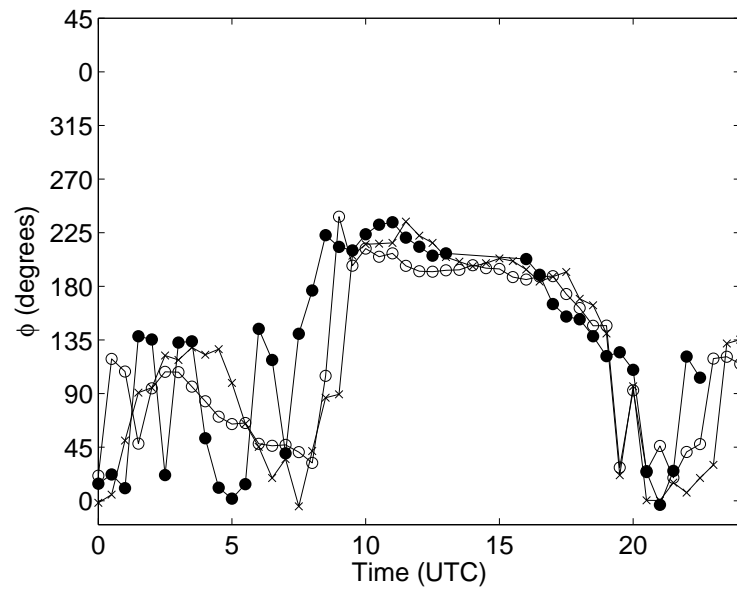


(b)

Figure 6: Surface data time series comparisons at Pian Perdascio (site C, on western slope) for (a) wind speed and (b) wind direction. —●— Observations at 5 m agl; —○— LU-SM; —×— REF-ST



(a)



(b)

Figure 7: Surface data time series comparisons at Monte Nuovo (site E2, on eastern slope) for (a) wind speed and (b) wind direction. —●— Observations at 22.7 m agl; —○— LU-SM; —×— REF-ST

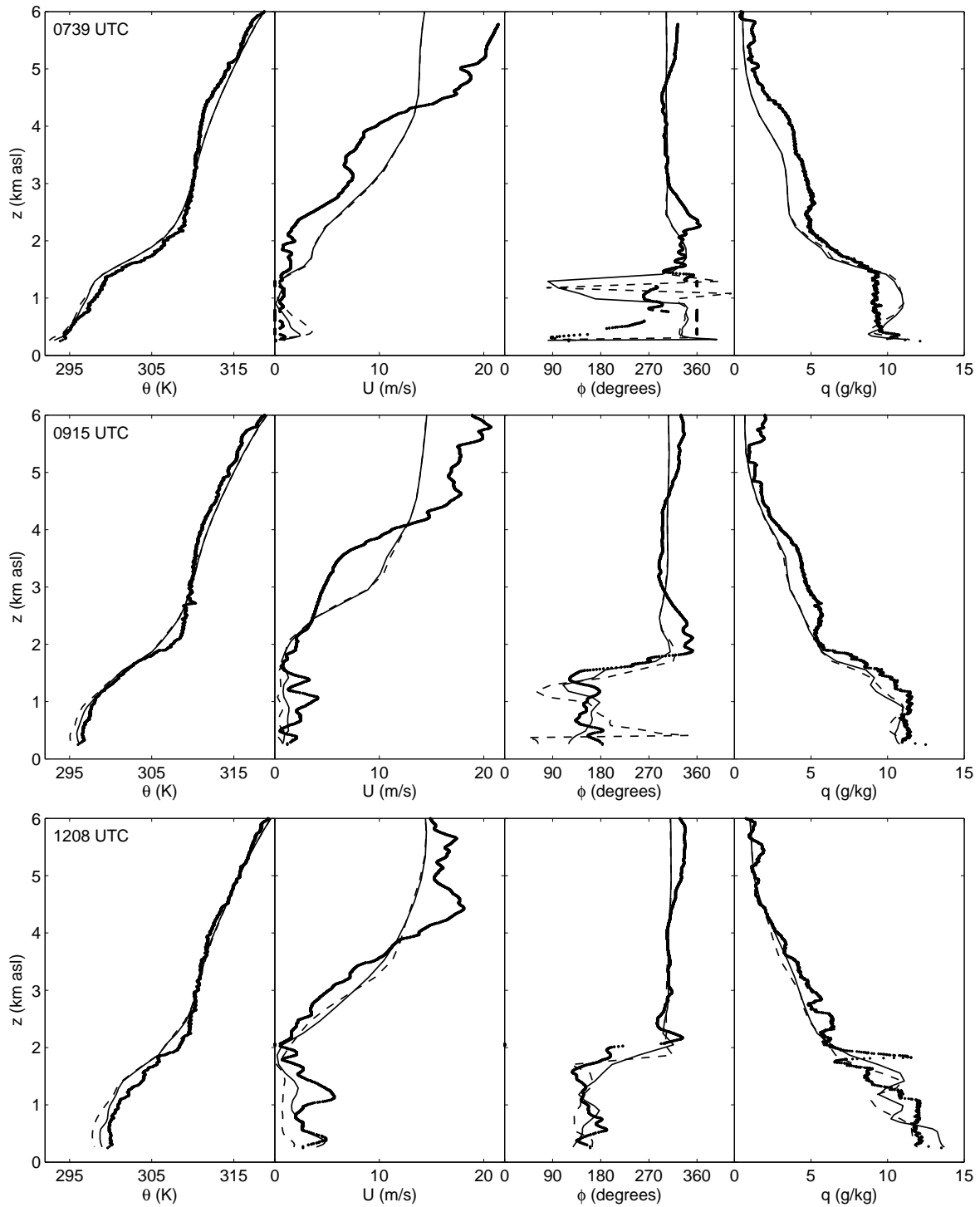


Figure 8: 0739, 0915, and 1208 UTC radiosonde observations compared to simulations at Bosco di Sotto (site A1) of potential temperature, wind speed, wind direction, and specific humidity on 25 August, 1999. Note that ϕ is equivalent to $\phi + 360$ Observations; —— LU-SM; ---- REF-ST

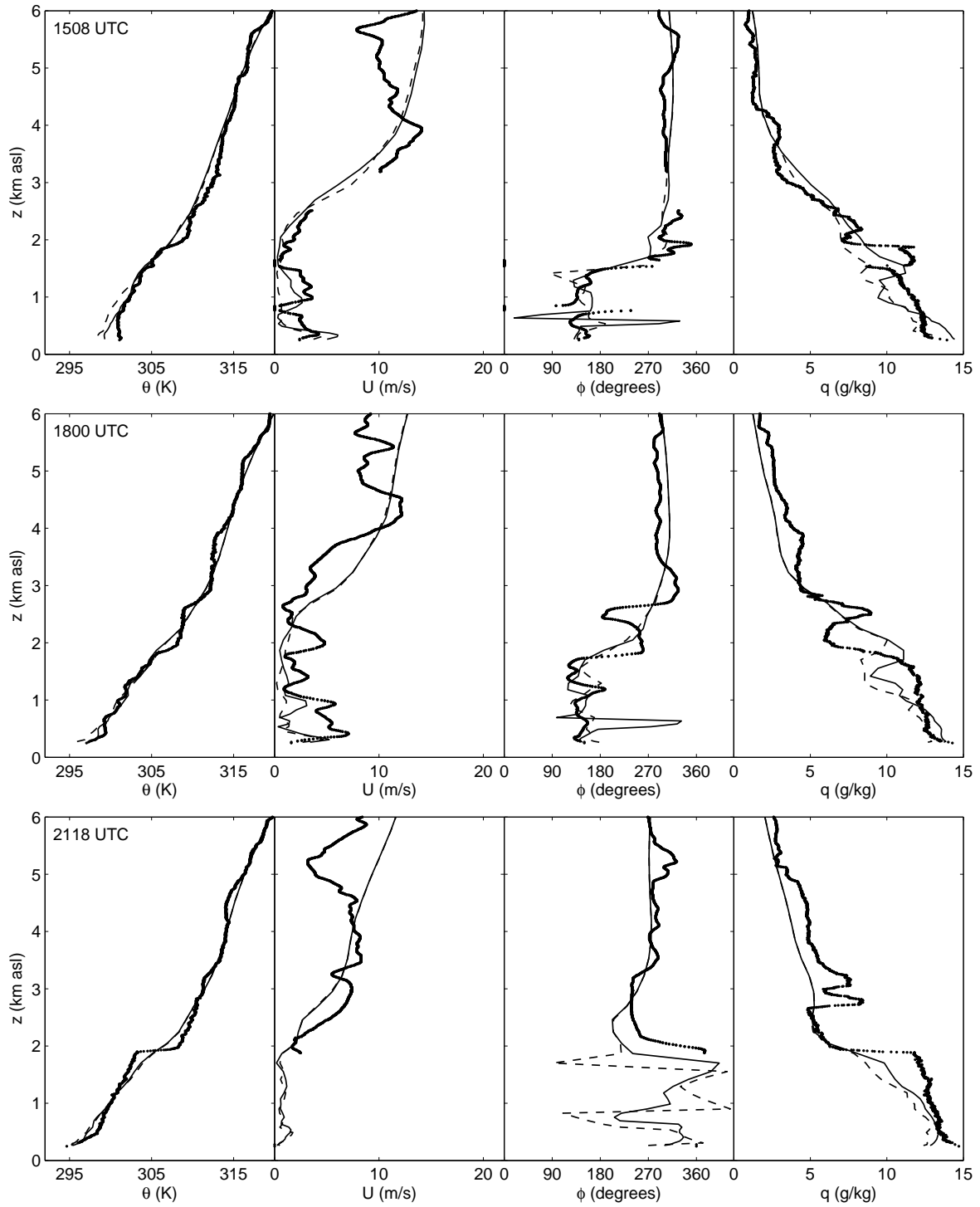
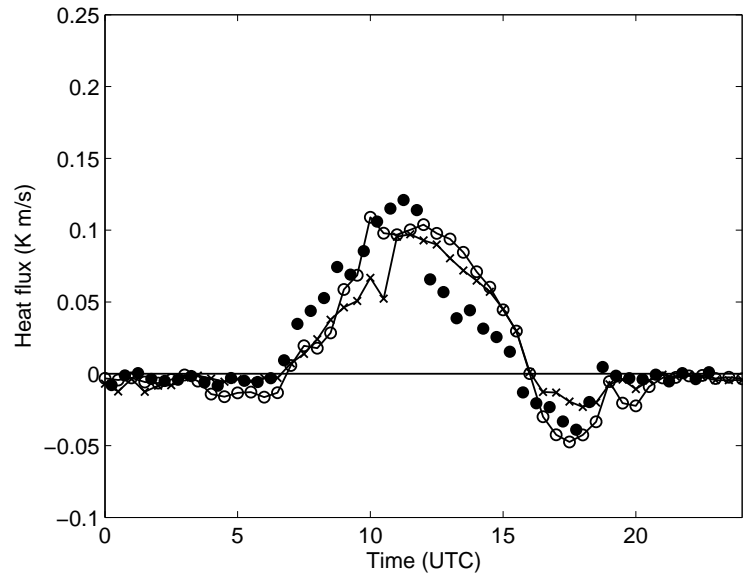
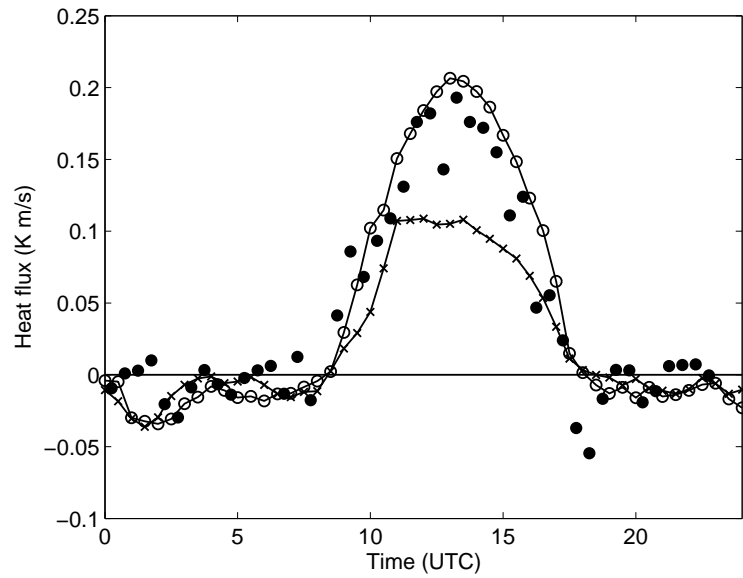


Figure 8: Continued for 1508, 1800, and 2118 UTC.



(a)



(b)

Figure 9: Time series of kinematic sensible heat ($\overline{w\theta}$) flux at (a) site A1 (valley floor) and (b) site B (eastern slope). • Observations; —○— LU-SM; —×— REF-ST.

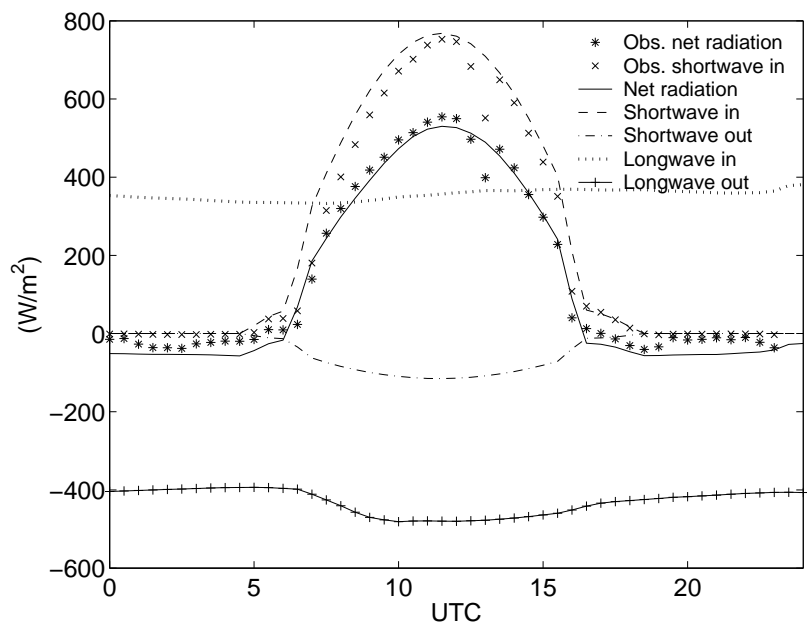


Figure 10: Radiation budget components from LU-SM compared to observations at site A1.

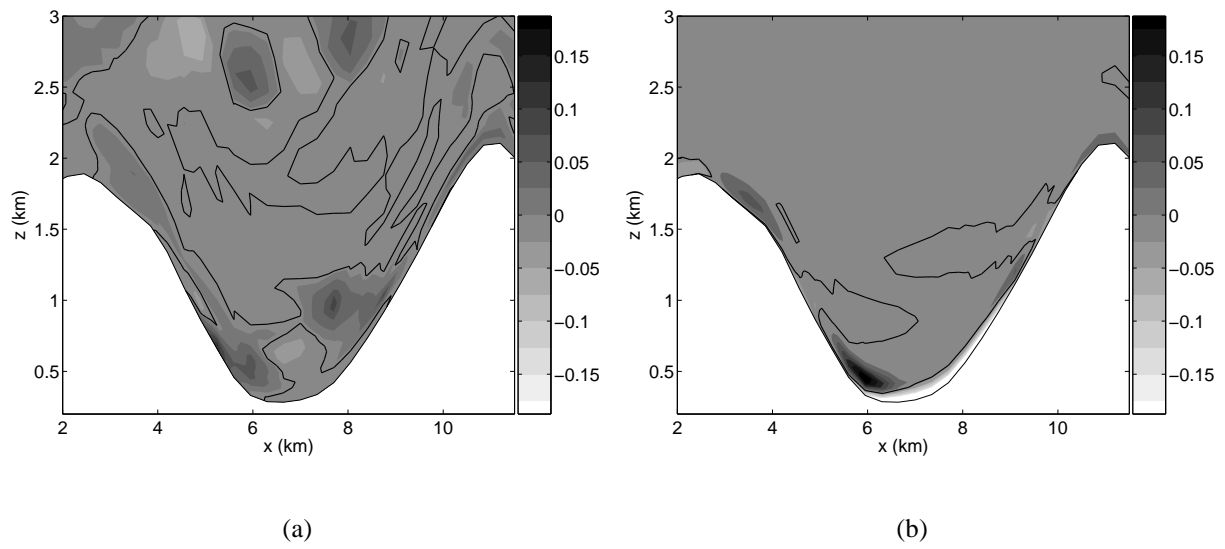


Figure 11: Vertical cross-sections of (a) resolved vw and (b) SFS τ_{23} stress (m^2/s^2) perpendicular to valley axis at site A1 for LU-SM. Time averaged between 1300 and 1500 UTC at 300 s intervals. The black contour line marks the zero contour.

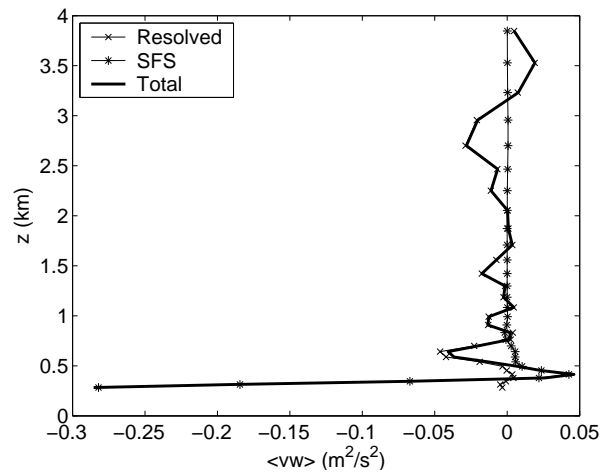
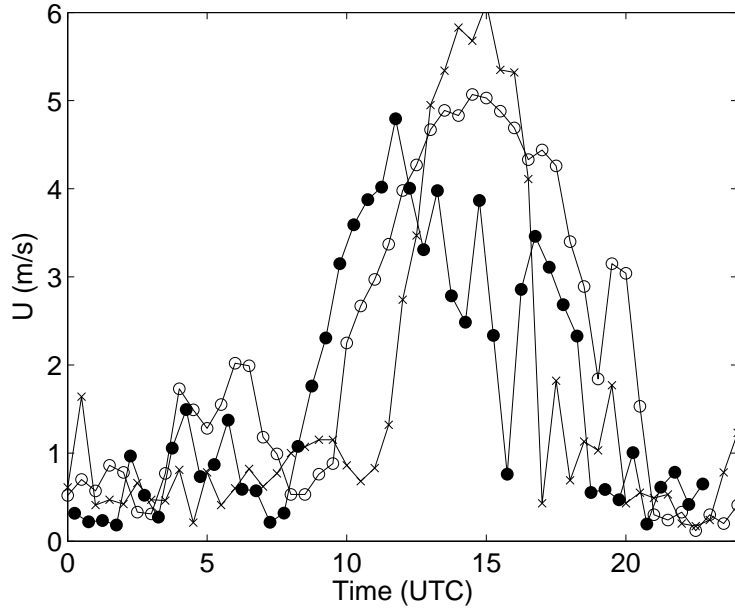
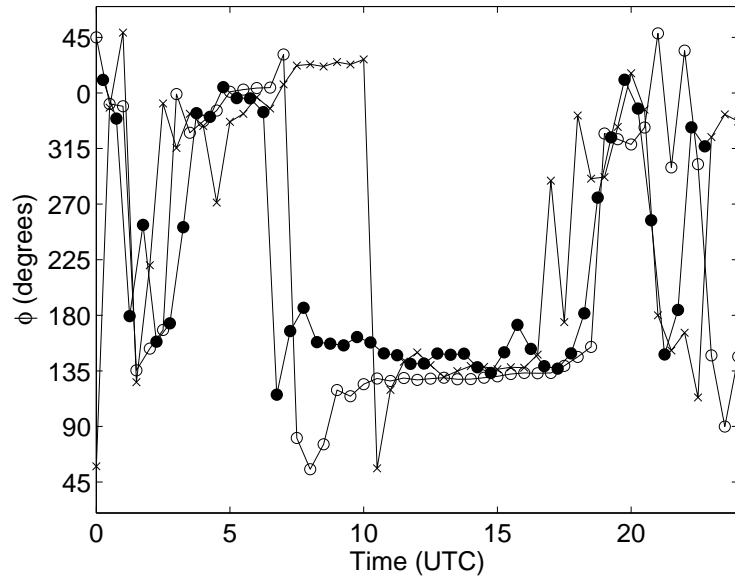


Figure 12: Vertical profile of resolved, subfilter-scale, and total stress for vw located on valley floor for LU-SM. Time averaged between 1300 and 1500 UTC at 300 s intervals.



(a)



(b)

Figure 13: Surface wind speed and direction at Bosco di Sotto (site A1) using different soil moisture initializations. —●— Observations; —○— LU-SM; —×— LU-SM2

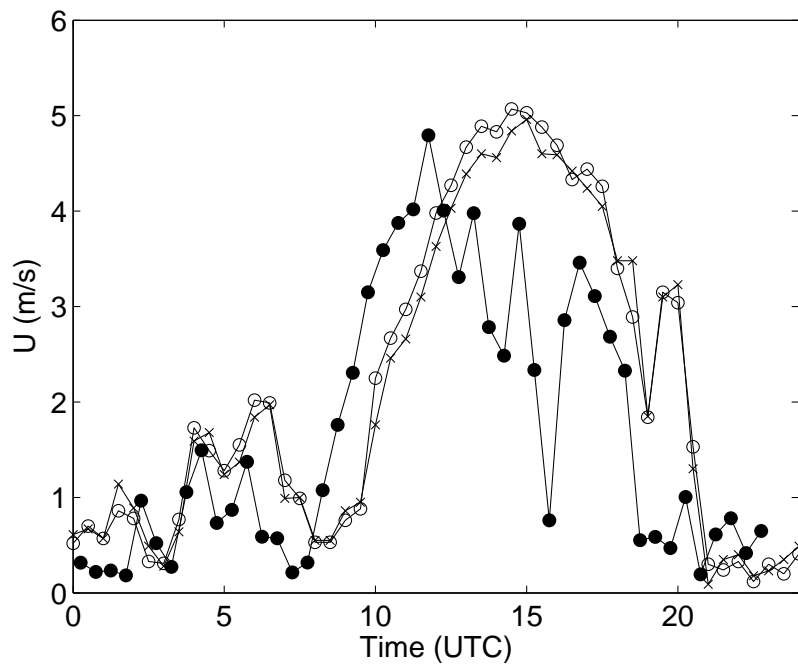
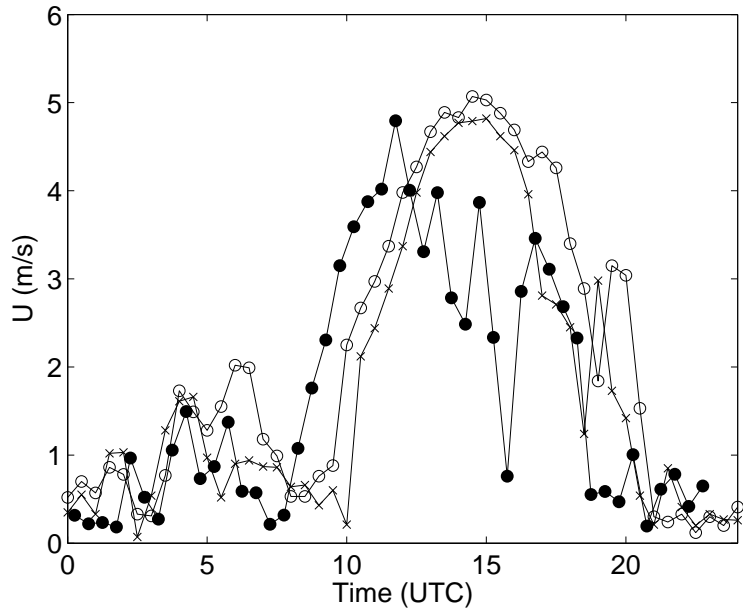
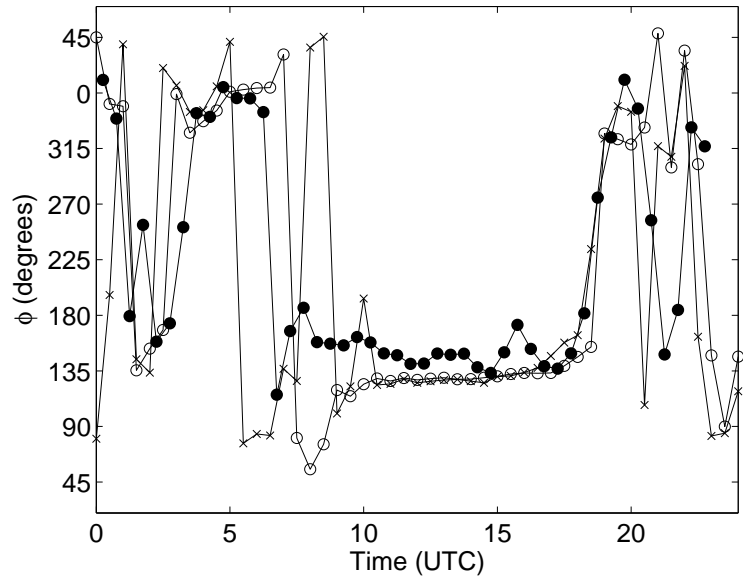


Figure 14: Surface wind speed at site A1 using different soil moisture initializations. —●— Observations; —○— LU-SM; —×— LU-SM3



(a)



(b)

Figure 15: Surface wind speed and direction at Bosco di Sotto (site A1) using different land use data. —●— Observations; —○— LU-SM; —×— SM

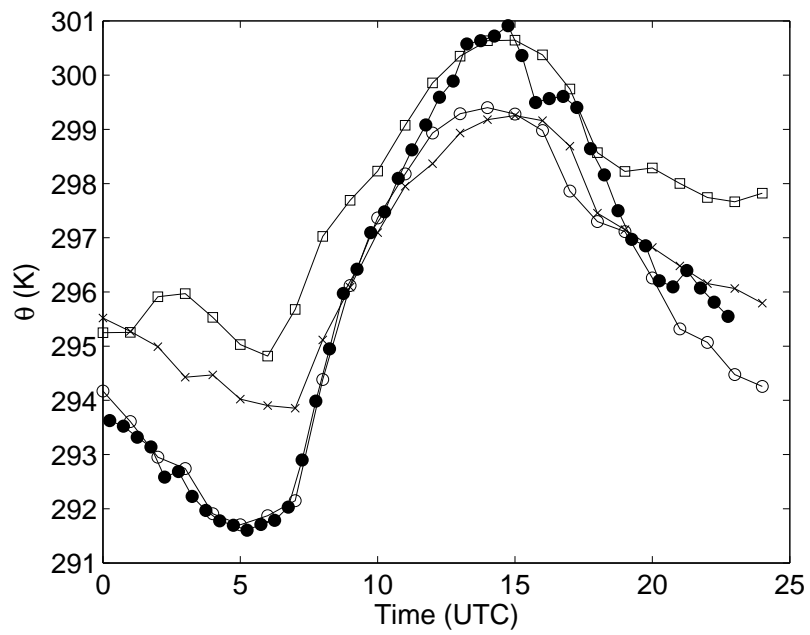


Figure 16: Surface potential temperature at site A1 at various grid resolutions for LU-SM.
 —●— Observations; —□— 3 km; —×— 1 km; —○— 350 m

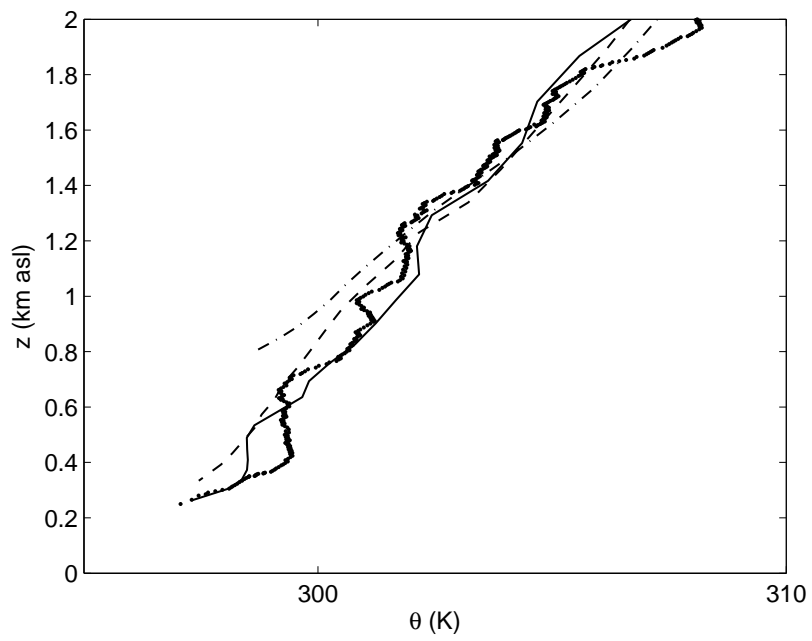


Figure 17: Close-up of potential temperature soundings at 1800 UTC and various grid resolutions for LU-SM. Observations; -.-.- 3 km; - - - - 1 km; ——— 350 m.

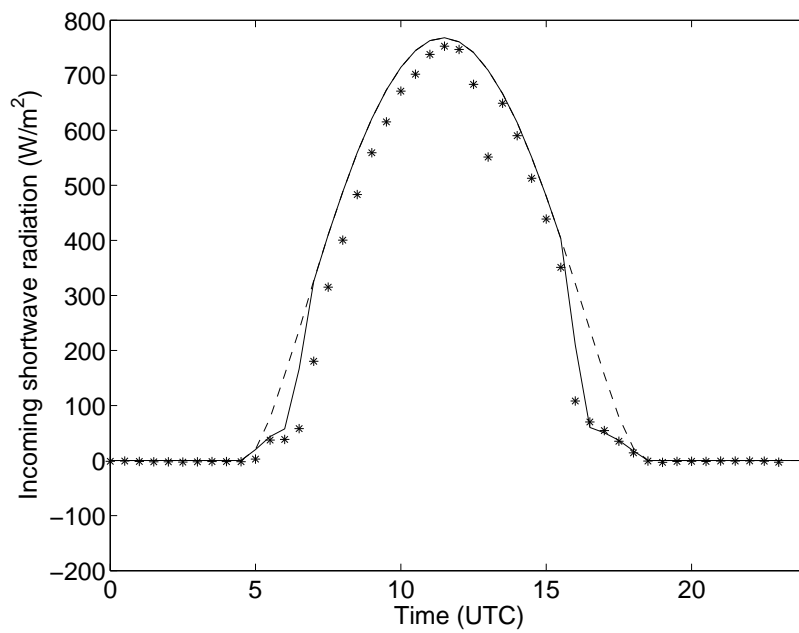


Figure 18: Incoming solar radiation, with and without topographic shading, at site A1. * Observations; — LU-SM; ---- LU-SM-NOSHADE

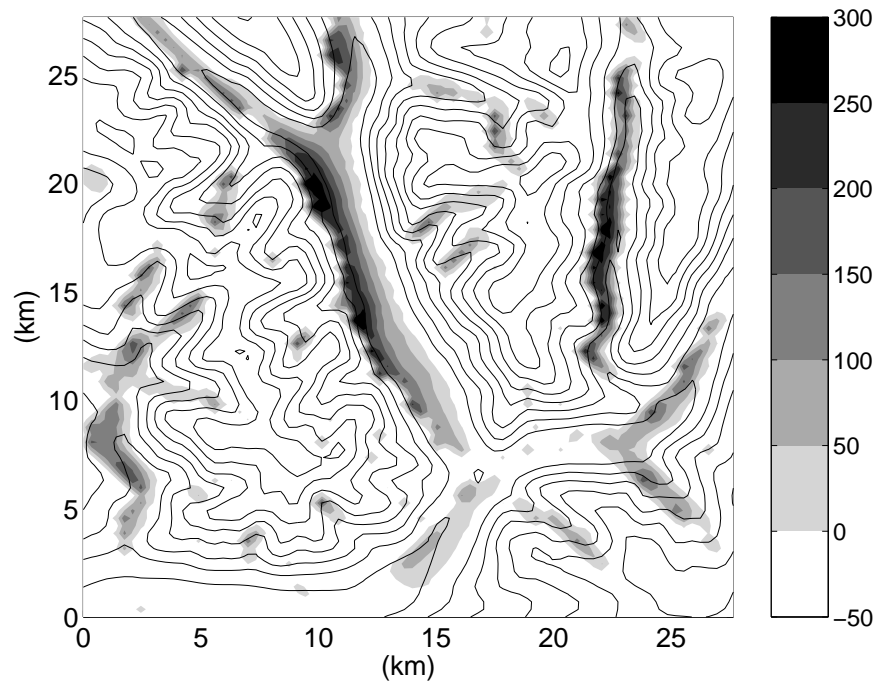


Figure 19: Difference in shortwave incoming radiation (filled contours, W/m^2) with and without shading (LU-SM-NOSHADE minus LU-SM) for the 350 m grid at 0600 UTC. Elevation contours (lines) shown at 250 m intervals.

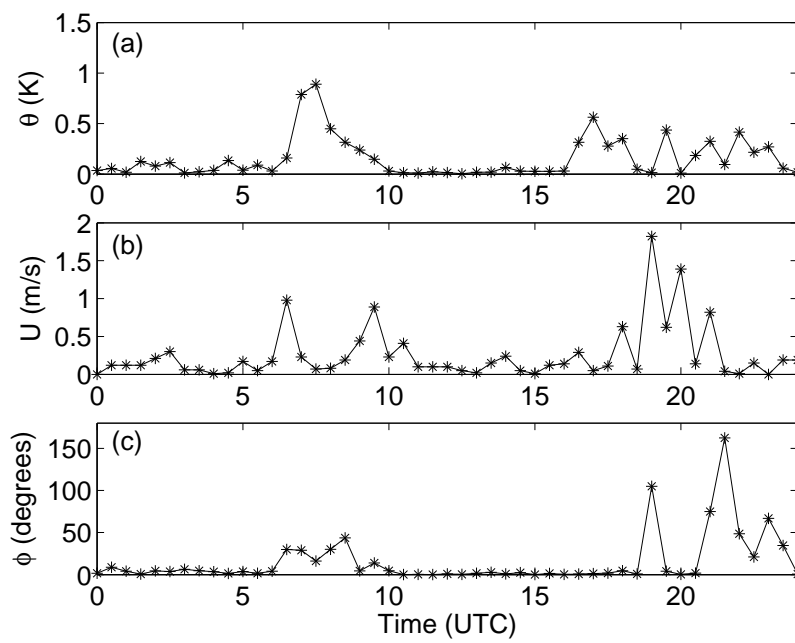
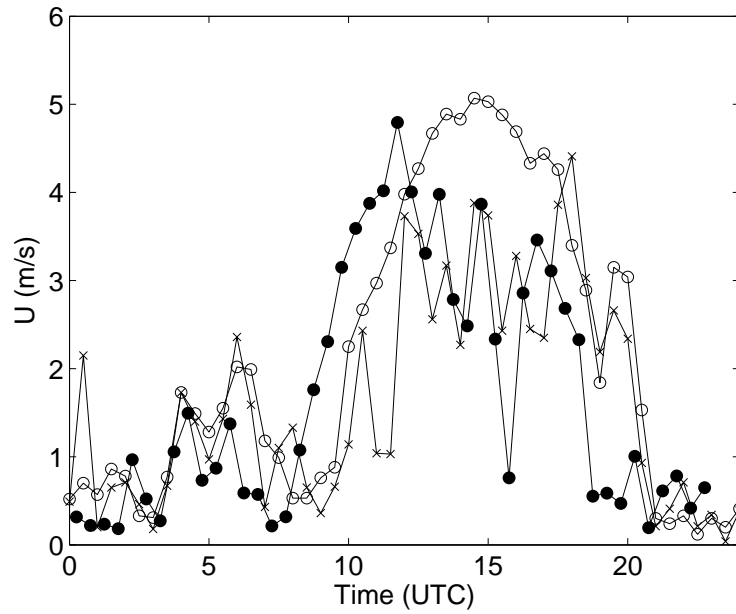
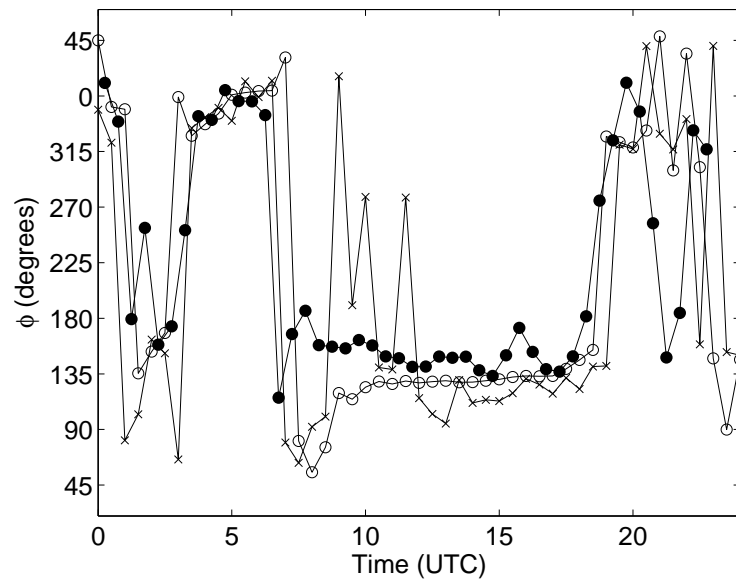


Figure 20: Time series of the absolute difference between LU-SM and LU-SM-NOSHADE surface variables at site A1 for (a) potential temperature, (b) wind speed, and (c) wind direction.



(a)



(b)

Figure 21: Surface wind time series comparisons with and without a turbulence model at Bosco di Sotto (site A1) for (a) wind speed and (b) wind direction. —●— Observations; —○— LU-SM; —×— LU-SM-NOTURB

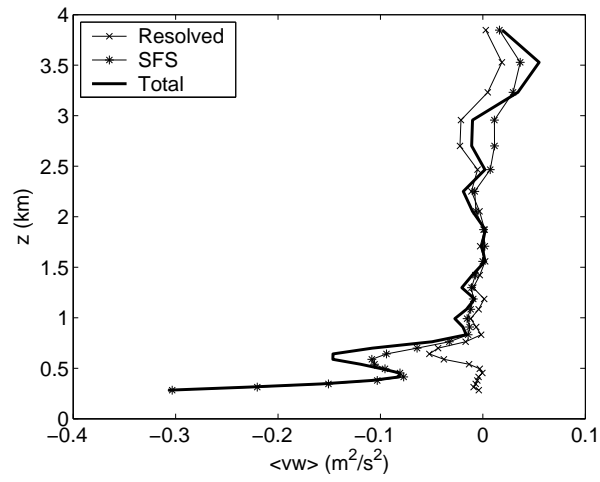
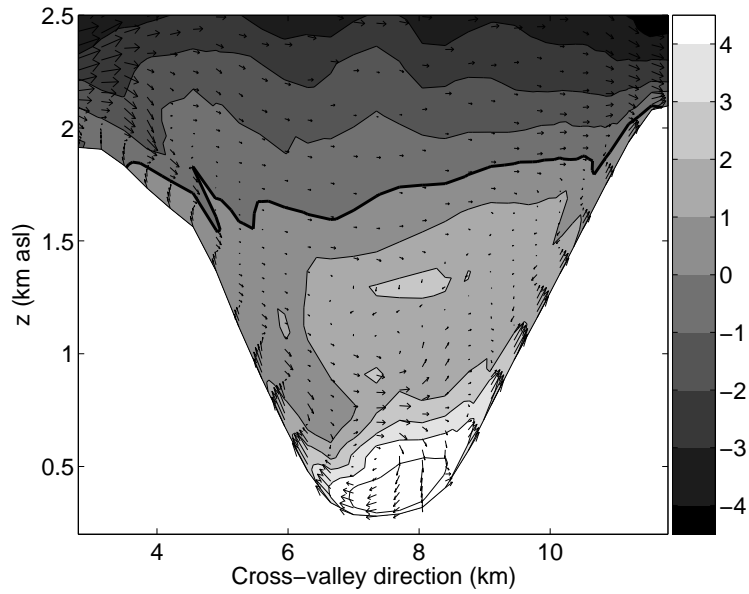
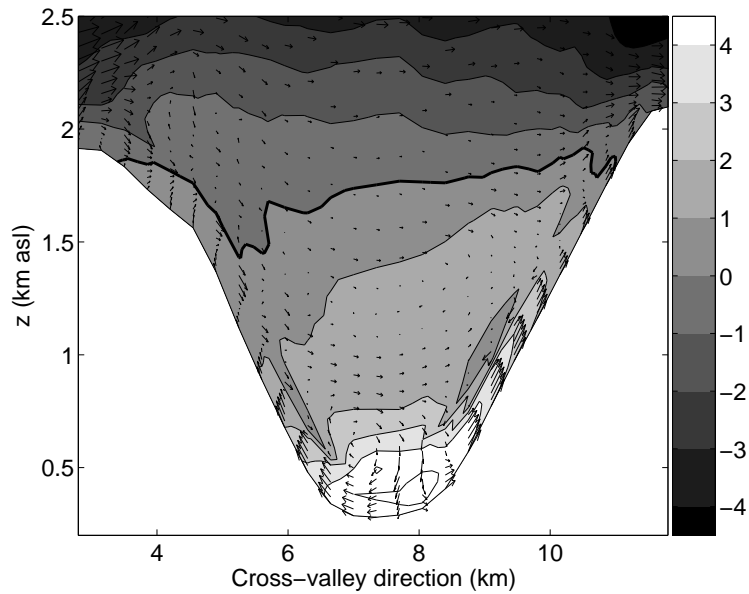


Figure 22: Vertical profile of resolved, subfilter-scale, and total stress for vw at the valley floor for LU-SM-DRM (using the DRM turbulence closure). Time averaged between 1300 and 1500 UTC at 300 s intervals.



(a)



(b)

Figure 23: Cross-valley winds (vectors) and along-valley winds (m/s, shaded) at 1300 UTC from the 350 m grid for (a) LU-SM with TKE-1.5 and (b) LU-SM-DRM with the DRM turbulence closure. Simulations start at 1200 UTC using identical initial and boundary conditions. Cross-valley distance measured along line shown in Fig. 2b. The zero contour line is shown in bold.